Topographic, spectral and thermal inertia analysis of interior layered deposits in Iani Chaos, Mars

E. Sefton-Nash [a,*], D.C. Catling [b], S.E. Wood [b], P.M. Grindrod [c,d], N.A. Teanby [a]

[a] School of Earth Sciences, University of Bristol, Wills Memorial Building, Queen's Road, Bristol BS8 1RJ, UK
[b] Department of Earth and Space Sciences, University of Washington, 4000 15th Avenue NE, Seattle, WA 98195, USA
[c] Department of Earth Sciences, University College London, Gower Street, London WC1E 6BT, UK
[d] Centre for Planetary Sciences, University College London, Gower Street, London WC1E 6BT, UK

ABSTRACT

We present an analysis of Interior Layered Deposits (ILDs) in Iani Chaos using visible, infrared, hyperspectral and topographic datasets acquired by instruments aboard NASA's Mars Global Surveyor, Mars Odyssey, Mars Reconnaissance Orbiter and ESA's Mars Express spacecraft. We focus on four main regions where ILDs outcrop in Iani Chaos. Deposits span a ~2 km range of elevations and exhibit moderate to high albedos, layering at sub-decameter scales, thermal inertias of 300–800 J m^{-2} K^{-1} s$^{-1/2}$ and a range of surface textures. Thermal inertia calculations use slope and azimuth corrections from High Resolution Stereo Camera (HRSC) topography. Spectral features in hyperspectral data acquired by NASA's Compact Reconnaissance Imaging Spectrometer for Mars (CRISM) suggest that gypsum (CaSO$_4$·2H$_2$O) and kieserite (MgSO$_4$·H$_2$O) are present in most deposits. We report absorptions typically exhibited by alunite (KAl$_3$(SO$_4$)$_2$(OH)$_6$) and jarosite $\left(KFe_3^{3+}(OH)_6(SO_4)_2\right)$ as well as a number of features that may be attributable to a wide range of mono- and polyhydrated sulphates and hydroxyl-sulphates bearing a number of cations, including Mg^{2+}, Fe^{2+}, Fe^{3+} and Ca^{2+}. Spectral features similar to those of ammonium sulphates may also be present.

Analysis of a HiRISE stereo DEM shows planar layering in some ILDs, favouring a sedimentary deposition origin. Stratigraphic mapping of hydration and sulphate spectral features in flat ILDs in central Iani Chaos suggest that specific elevation intervals in the stratigraphic column were subject to different levels of hydration, perhaps during episodes of water table elevation. This is consistent with formation models for ILDs and hydrological modelling. Geomorphic characteristics of deposits in northern and southern Iani Chaos suggest their relatively recent exhumation and significant erosion by aeolian processes. We conclude that any formation theory for ILDs in Iani Chaos should support mechanisms for different hydration states at different stratigraphic elevations and subsequent significant aeolian erosion, burial and re-exposure.

1. Introduction

The martian circum-Chryse outflow channel systems appear to be some of the most fluvially altered terrains on the planet. They are generally sourced by chaotic terrains, which comprise fractured regions, jumbled blocks, mesas separated by channels and low-elevation plains scattered with debris (Sharp, 1973). Areas of chaotic terrain towards the eastern end of the Valles Marineris system are thought to show a diverse, multi-episodic outflow history (Warner et al., 2009; Carr and Head, 2010). Iani Chaos, centred approximately at 342°E, 2°S, is of importance because it is thought to be a main source region for fluids produced in catastrophic floods that carved Ares Vallis (Baker and Milton, 1974), a ~1500 km outflow channel that has cut through Noachian and early Hesperian cratered plateaus (Pacifici et al., 2008), and connects northern Iani Chaos to the Chryse Basin (Fig. 1a).

Morphological analyses of the mouth of Ares Vallis (Marchenko et al., 1998) and syngenetic erosional features in and surrounding the channel (Warner et al., 2009, 2011) suggest that Ares Vallis was carved by multiple large-scale floods. Episodic fluid release is also supported by aquifer modelling of the Uzboi–Ladon–Margaritifer mesoscale outflow system (Harrison and Grimm, 2008). However, the cause of the outflow process (generally considered to be a large release of water causing subsidence, collapse and, ultimately, the formation of chaotic terrain) is still poorly constrained. Hypotheses include melting of permafrost, or de-watering of hydrated sulphates (Montgomery and Gillespie, 2005), during periods of warmer climate, magmatic activity or impact events. One alternative
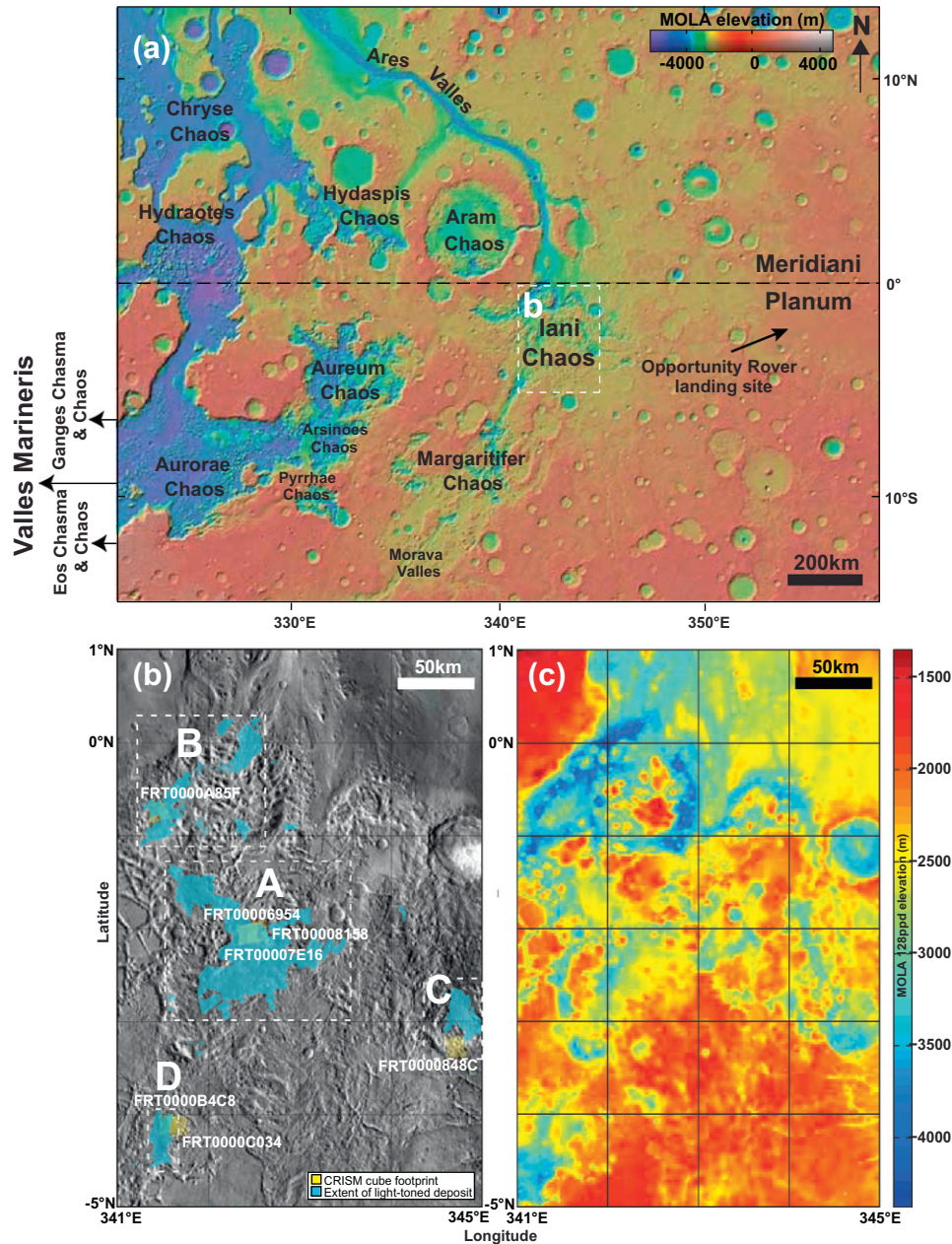
Fig. 1. Setting of Iani Chaos and interior layered deposits. (a) Relief-shaded and colourised 128 pixel per degree MOLA elevation data of the region East of the Valles Marineris. The area outlined by the dashed white box is displayed as panel 'b'. (b) The location of the interior layered deposits in Iani Chaos that were mapped (blue) with the location of CRISM cubes used in this study (yellow). The main mapping areas are labelled A–D. The background is a THEMIS daytime infrared mosaic. Dashed white boxes show the location of panels in Fig. 2. (c) 128 pixel per degree MOLA topography for the same geographic extent as panel b. (For interpretation of the references to colour in this figure legend, the reader is referred to the web version of this article.)

school of thought attributes outflow channels to very fluid lavas (Leverington, 2011). In any case, evidence suggests that Iani Chaos probably acted as a reservoir and conduit for processes involving fluid sourced from outflow events until the mid-Hesperian. The resulting landscape is a mixture of jumbled blocks, mesas, channels and low elevation landscapes littered with debris. Interior layered deposits (ILDs) are exposed in these terrains.

ILDs have been an enigmatic feature of the martian sedimentary record, since their mineralogy and morphology appear to have been mediated by the presence of fluids. ILDs have been proposed to be fluvial (Ori and Mosangini, 1998), glacial or lacustrine (Malin and Edgett, 2000) sediments. Other works concluded that they could have formed by sub-aerial volcanic deposition (Peterson, 1981; Lucchitta, 1990), dust deposition on ice-covered lakes

(Nedell et al., 1987), deposition in meltwater by sub-ice volcanoes (Chapman and Tanaka, 2001; Komatsu et al., 2004) or large scale deposition by springs (Rossi et al., 2008). More recent theories include formation by diagenesis of aeolian sediments during episodic groundwater upwelling (Murchie et al., 2009; Andrews-Hanna et al., 2010), acid weathering of dust and sand trapped with volcanic aerosols in massive ice deposits during successive periods of high obliquity (Niles and Michalski, 2009), and build up of groundwater precipitates facilitated by topographic pumping (Grindrod and Balme, 2010). In many theories, ILDs are proposed to have undergone diagenesis during conditions that enable the stability of liquid water or brines. The final stage of ILD formation is thought to generally be aeolian erosion during the recent Amazonian (Warner et al., 2011).
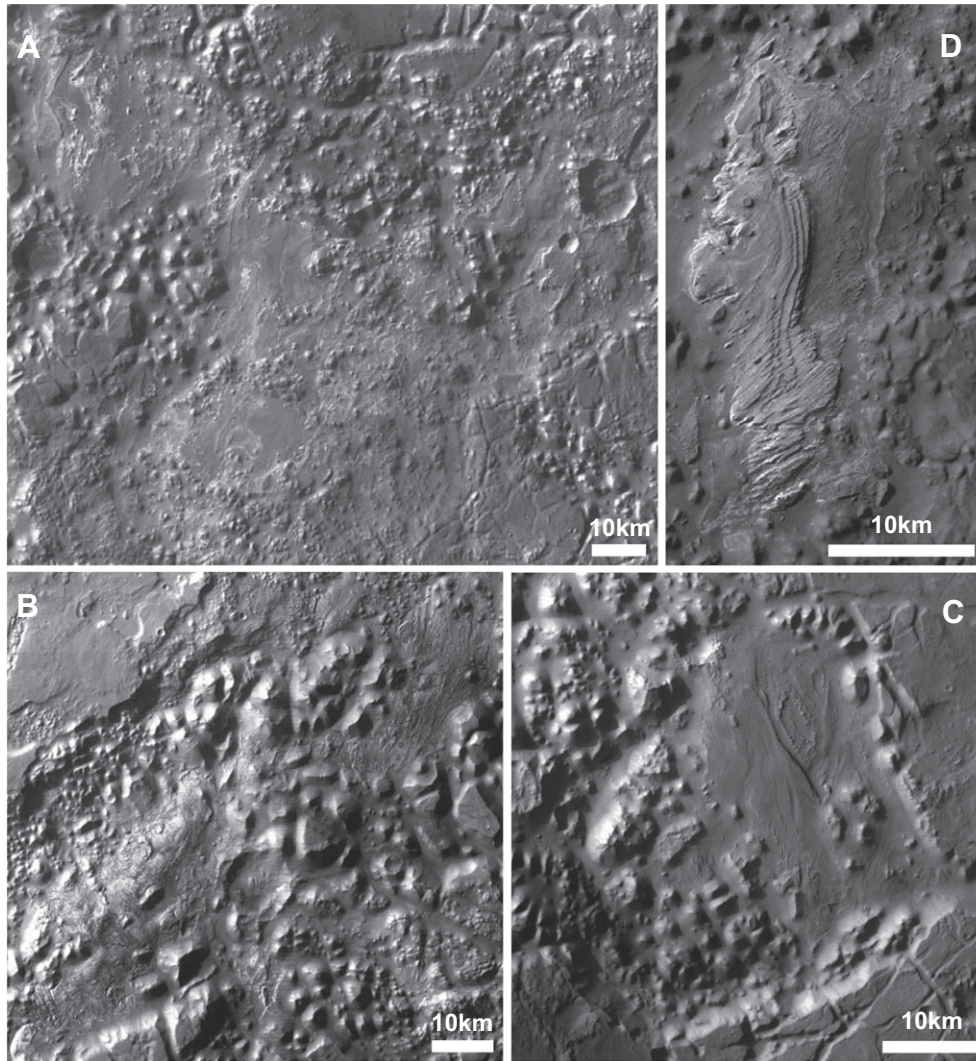
Fig. 2. The main ILD-bearing regions in Iani Chaos, which we designate A–D. The areas covered by each panel are shown as white dashed boxes in Fig. 1. Images are the nadir channel of HRSC (spatial resolution of 12.5 m/pixel). Sources are as follows: A – H4134_0000_ND3, H0923_0000_ND3 and H0934_0000_ND3. B – H0934_0000_ND3. C – H0901_0000_ND3. D – H0934_0000_ND3. Where multiple products are listed, they have been mosaicked.
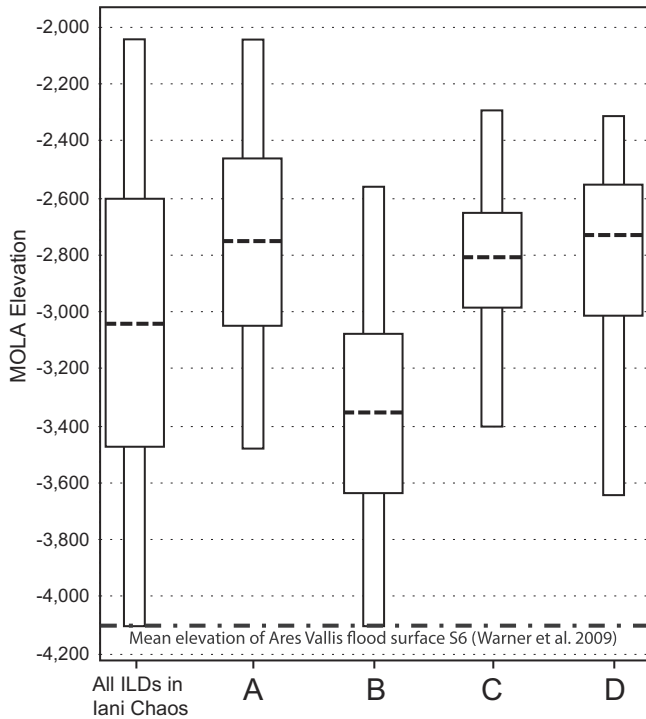
2. ILDs in Iani Chaos

ILDs in Iani Chaos show layering on multiple scales (Bridges et al., 2008; Warner et al., 2011), exhibit higher thermal inertias than surrounding terrains (Glotch and Rogers, 2007) and are sometimes topped by dark 'cap' units, similar to those in Juventae Chasma (Catling et al., 2006), Aram Chaos (Catling and Moore, 2003; Glotch and Rogers, 2007), Mawrth Vallis (Loizeau et al., 2010) and Valles Marineris (Komatsu et al., 2004). ILDs are almost always associated with detections of sulphate minerals, which are often hydrated (Bibring et al., 2006; Bishop et al., 2009; Gendrin et al., 2005), and some are reported to show spectral features indicative of phyllosilicates (Grindrod et al., 2012; Weitz et al., 2011). Boulders and talus at the base of ILD slopes show active mass-wasting. The lack of small craters and the presence of features caused by aeolian erosion on ILD surfaces suggests that they have been relatively recently exhumed and are being actively eroded by the wind.

We map the extents of the major deposits and surrounding outliers using a variety of high spatial resolution datasets. We used narrow angle images at 1.5 m/pixel from the Mars Orbital Camera (MOC) aboard NASA's Mars Global Surveyor and IR/VIS images (at 100 and 10 m/pixel, respectively) from the Thermal Emission Imaging Spectrometer (THEMIS) aboard NASA's Mars Odyssey. Both of these datasets have been previously used for mapping ILDs in Iani Chaos (Glotch and Rogers, 2007). We also include pan-chromatic images at 12.5–175 m/pixel from the High Resolution Stereo Camera (HRSC) aboard ESA's Mars Express and mono-chromatic images from the Context Imager (CTX, 5 m/pixel) and High Resolution Imaging Science Experiment (HiRISE, 0.25–0.5 m/pixel) instruments aboard NASA's Mars Reconnaissance Orbiter. ILD boundaries were mapped at the resolution of the available imagery using a geographic information system. Regions containing significant ILDs are shown as the filled blue areas labelled A–D in Figs. 1b and 3. Areas within boundaries do not contain 100% ILD exposure, due to partial coverage by dust and dune-forming material. In general boundaries contain areas where ILDs comprise the predominant exposure.

2.1. Topography

We map ILD boundaries and extract surface elevations within them from 128 pixel per degree (~460 m/pixel) gridded data obtained by the Mars Orbiter Laser Altimeter (MOLA) (Fig. 1c). The elevation distribution for each ILD region and for all regions is

Fig. 3. Box and whisker plot displaying range of elevations covered by ILDs mapped in Iani Chaos, according to MOLA global 128ppd gridded data. A–D represent the topographic distribution of the ILDs as mapped in blue in Fig. 1. The central dashed line represents the mean, the top and base of each wide box mark the upper and lower quartiles of the distribution and the upper and lower extents of the whiskers indicate the maximum and minimum elevations. The left-most symbol represents the distribution for all regions. The mean elevation of the flood surface S6 (Warner et al., 2009) at the head of Ares Vallis is also marked by a dashed-dotted line.

plotted in Fig. 3. Compared to chaotic terrains to the immediate East of the Valles Marineris system, Iani Chaos is shallower and appears less excavated. ILDs in regions A, C and D occupy similar elevation ranges lying between −2000 and −3600 m, with an average elevation around −2800 m. Region B shows a lower average of approximately −3350 m, as it is situated in a topographic depression that contains the lowest point in Iani Chaos, ∼800 m below the head of Ares Vallis (Pacifici et al., 2008). We find our elevations

generally in agreement with those made by Warner et al. (2011) using a 40 m/pixel stereo-derived DTM of Iani Chaos constructed from HRSC images (Gwinner et al., 2010).

2.2. Thermophysical properties

Thermal inertia derived from remotely-sensed infrared data provides an important measure of the bulk physical properties of surface geologic materials. Thermal inertia ($J\,m^{-2}\,K^{-1}\,s^{-1/2}$) is defined as the square root of the product of thermal conductivity ($W\,m^{-1}\,K^{-1}$), bulk density ($kg\,m^{-3}$), and specific heat capacity ($J\,K^{-1}\,kg^{-1}$), ($\kappa\rho c$)$^{1/2}$.

Variations in thermal inertia are dominated by changes in thermal conductivity, κ, which can vary by a factor of up to 1000 due to variations in air pressure (in pore space), particle size and degree of cementation (see Wood, 2011 and appendix of Catling et al. (2006)). The elevation–related pressure change is smaller than the seasonal pressure variation (≈25%), and both variations have a smaller effect on thermal inertia than changes in particle size or degree of cementation (Presley and Christensen, 1997; Piqueux and Christensen, 2008). We would expect atmospheric pressure to decrease by about 14% over the ∼1.6 km elevation range shown for ILDs in Iani Chaos, and the effect would remain constant for deposits at a common altitude, so localised variations in derived thermal inertia, or those on flat terrain, should be due to variations in bulk geologic properties.

We derive best-fit thermal inertia using THEMIS infrared (IR) images and MOLA/HRSC topography for each ILD-bearing region in Iani Chaos. Our derivation of thermal inertia is according to the procedure described in Catling et al. (2006), which best-fits diurnal temperature curves to surface temperatures derived from spatially coincident THEMIS IR day-night image pairs. Modeled temperatures form lookup tables for surface materials with a range of thermophysical properties (thermal inertia and albedo) and in a range of orientations (slope and azimuth). Synthetic surface temperatures are produced for a range of terrains using a modified version of the Kieffer model (Kieffer et al., 1977). For day images, surface temperatures are retrieved by assuming that brightness temperature of band 3 (7.93 μm) is equal to surface kinetic temperatures, because average TES-derived emissivity at this wavelength is very close to 1 (Bandfield, 2003). THEMIS band 3 is normally not acquired for night images, so to retrieve the surface kinetic temperatures the daytime ratio of band 4 to band 3 is calculated in the

Table 1

Details of HRSC and THEMIS data used in derivation of best-fit thermal inertia. 9.35 μm dust opacities that are reported here were retrieved for daytime images (when dust aerosols have the largest effect). Daytime images have a white row background while night images have a grey row background. Further validation of the thermal inertia data comes from knowledge of each image's solar longitude of acquisition, since the attenuating effects of the seasonal dust storms and the aphelion water–ice cloud belt are well characterised. Images acquired within the range $\sim20° \leqslant L_s \leqslant \sim 180°$ at this latitude are more likely to be affected by H_2O–ice in the aphelion cloud belt and those in the range $180° \leqslant L_s \leqslant 360°$ are noted as at risk from the dust storm season during northern Hemisphere winter. In general, dust aerosols tend to be more of an issue for day images while the effects of water–ice are more dominant for night images. However individual observations may be subject to conditions outside this norm.

Region	Thermal inertia range	HRSC topography	THEMIS ID	L_s	Possible seasonal aerosols	Dust opacity (9.35 μm)
A	500–700	H0923_0000_DT4	101773013	10.24	–	0.14
			105712007	159.75	Aphelion H_2O–ice cloud belt	–
Bl	550–700	H0401_0001_DT4	101798006	11.23	–	0.14
			107210007	231.79	Dust storm season	–
B2	550–700	H0923_0000_DT4	110648017	30.75	Aphelion H_2O–ice cloud belt Dust storm season	0.15
			117868017	345.64	Dust storm season	–
C	500–700	H0901_0000_DT4	106554021	198.69	Dust storm season	0.19
			129848008	123.03	–	–
D	550–700	H0401_0001_DT4	109425023	341.37	Dust storm season[a]	0.28
			118205017	359.82	Dust storm season[a]	–

[a] The image is less likely to be significantly affected by dust or water–ice opacity since it was acquired at the fringes of the seasonal period in which these phenomena are most active.
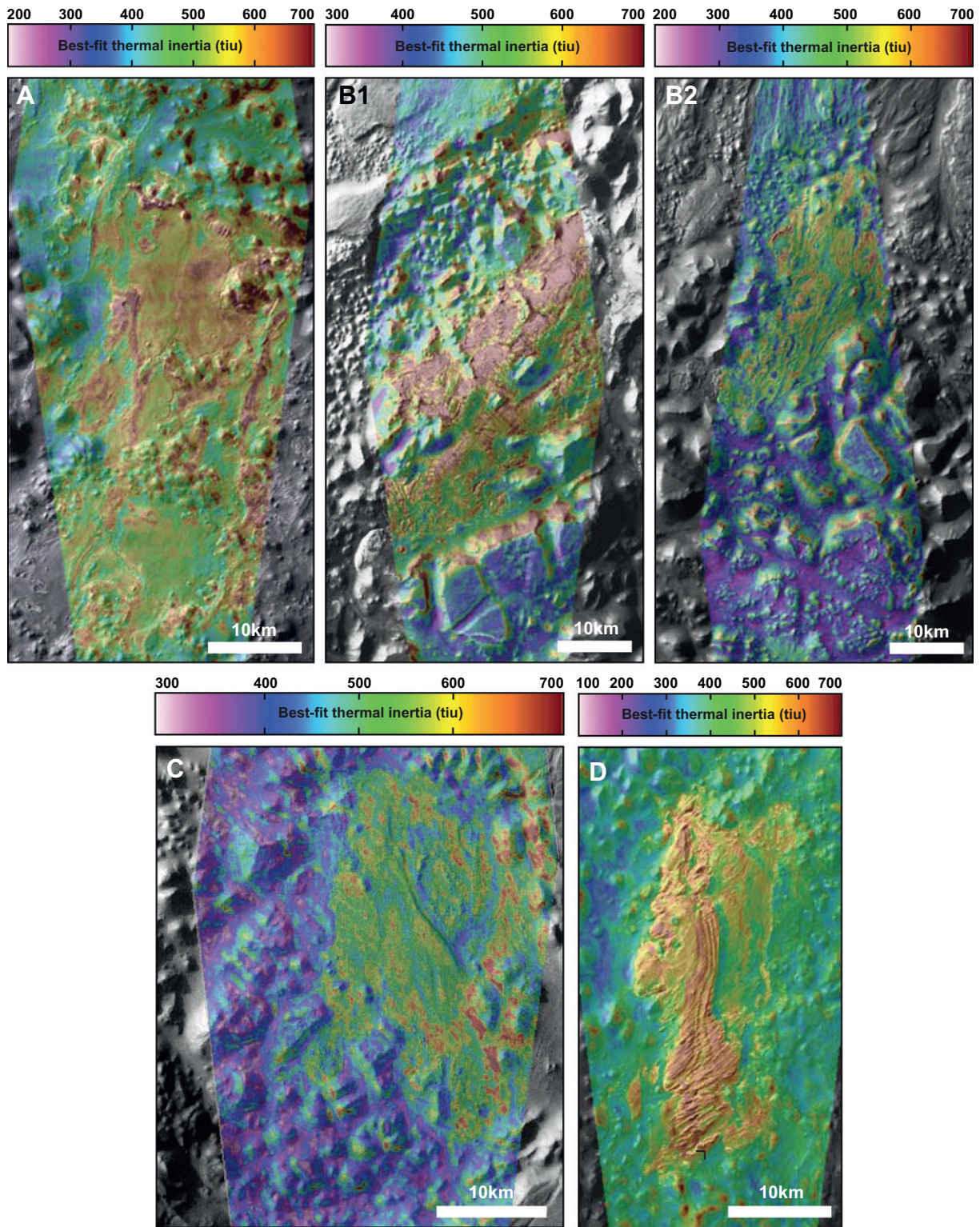
Fig. 4. Best-fit thermal inertia derived using the method described by Catling et al. (2006). Region labels are at the top left of each panel. Two main ILD outcrops in region B are labelled B1 and B2. Details of THEMIS images and HRSC topography used in the derivation of each thermal inertia map are listed in Table 1. Thermal inertia data is overlaid at 70% transparency on HRSC nadir channel imagery. North is up in every panel.

area of image overlap. The ratio is assumed to be equal to the emissivity at the wavelength of band 4 (8.56 μm) and is then used to solve for nighttime surface kinetic temperatures.

Surface kinetic temperature retrievals can be affected by the presence of atmospheric aerosols, such as dust and water–ice.

The seasonal distribution of periods of high opacity due to aerosols has been well documented using TES and THEMIS spectra (Smith et al., 2003) and dust opacities for daytime THEMIS images are routinely calculated as part of the processing pipeline. Thermal inertia estimates where the day image showed a high optical depth or
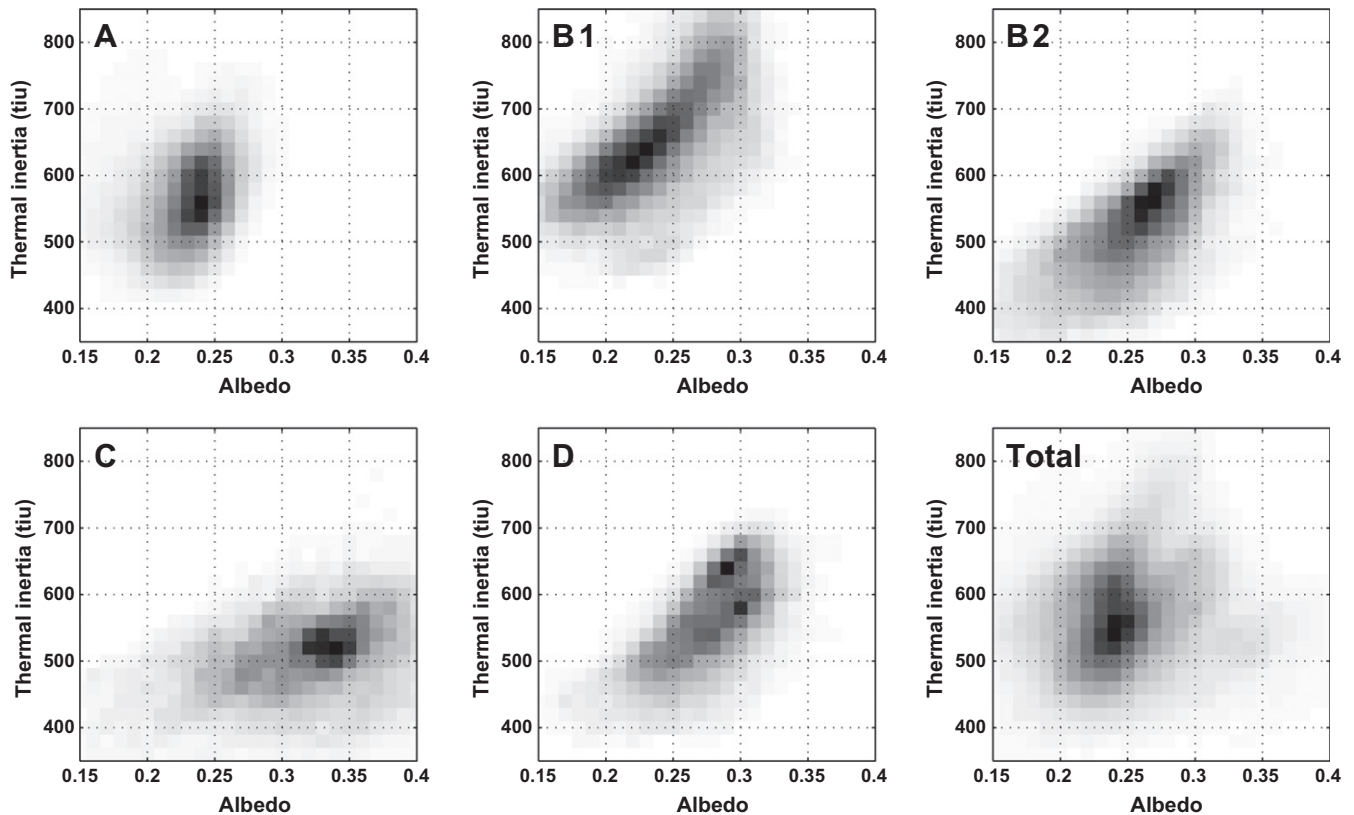
Fig. 5. Derived thermal inertia vs. derived albedo for ILDs in Iani Chaos. Thermal inertia bins are 20 tiu wide and albedo bins are 0.01 wide, to match the resolution of the lookup table generated by the thermal model. The binned quantities are the thermal inertia and albedo values of pixels that lie within the geographic boundaries of ILDs (as mapped in Fig. 1b). For all ILDs there is generally a positive correlation between thermal inertia and albedo. Notable variations between regions include a significantly lower thermal inertia of B2 compared to B1 and a higher than average albedo exhibited by deposits in region C.

where either image was acquired during a seasonal period with typically high concentrations of atmospheric aerosols were treated as less reliable. Table 1 shows the results of these estimates and images that are likely to be affected by seasonal aerosols.

Glotch and Rogers (2007) note that light-toned units in Iani Chaos show average TES thermal inertias of $\sim$320–360 J m^{-2} K^{-1} s$^{-1/2}$ (hereafter the S.I. unit for thermal inertia is abbreviated to tiu) compared to $\sim$260–300 tiu for the surrounding terrain. In general we observe a wider range of thermal inertias than has been previously documented for ILDs in Iani Chaos. This is largely due to the smaller size of THEMIS pixels (100 × 100 m) compared to TES pixels ($\sim$3 × 5 km), which works to reduce the spatial averaging that is inherent in TES thermal inertia data.

We derive a range of thermal inertias for ILDs in Iani Chaos that span 360–840 tiu, with a mean thermal inertia of $\sim$550 tiu and mean albedo of $\sim$0.24 (Figs. 4 and 5).

3. Individual analyses

3.1. Region A

Region A contains the most extensive interior layered deposits in Iani Chaos (Figs. 1 and 2A). ILDs in this region appear at a wide range of elevations: approximately −3500 to −2050 m (Fig. 3). At the centre of this region, protruding mounds, presumably formed or exposed in a chaos-forming event, are embayed at their bases by a sequence of beds that conform to topography (Gilmore and Greenwood, 2009).

Unlike ILDs in regions B and D, these deposits do not have surfaces dominated by pronounced wind-sculpted features. They

show an intermediate albedo and a crater retention age of $\sim$100 ± 25 Ma (Warner et al., 2011). The population distribution of small diameter craters (<500 m) for ILDs in region A is similar to that for B and D, but the crater retention age for ILDs in region A is roughly four times that for ILDs in regions B ($\sim$25 Ma) and D ($\sim$22 Ma) (Warner et al., 2011). The relatively high number of small craters and relative lack of aeolian erosional features for ILD A, despite its greater age than ILDs in regions B and D, may be related to resistance to wind erosion due to composition, thickness, or simply the absence of sufficiently strong winds at this location.

Cliffs composed of light-toned material show boulders and fine talus littering their bases (Fig. 6a), suggesting that the ILD is friable and being actively eroded. The cliff depicted in Fig. 6a and marked by white arrows in Fig. 7 strikes mostly N–S and, between the arrows, its upper surface drops in elevation by $\sim$1200 m to a sand sheet in a topographic depression (marked by the southernmost arrow). This could suggest that either the cliff-forming unit has a very large thickness, that it was laid down conforming to pre-existing topography that covered these extents or that the southern portion of the unit has been subject to erosion or subsidence since formation (relative to the northern portion).

The ILD in region A shows exposed contacts between beds, which appear to have varying erosional habits and albedos. Fig. 6b shows such a contact at a stratigraphically low position, between a smoother bed of relatively low albedo that lies beneath a sequence of layers that are topped with a scalloped surface. Minor dunes of dark material are seen to gather in the topographic depressions.

Putzig et al. (2005) report average TES-derived thermal inertias of $\sim$360 tiu and albedos of $\sim$0.18 for ILDs in region A (compared to
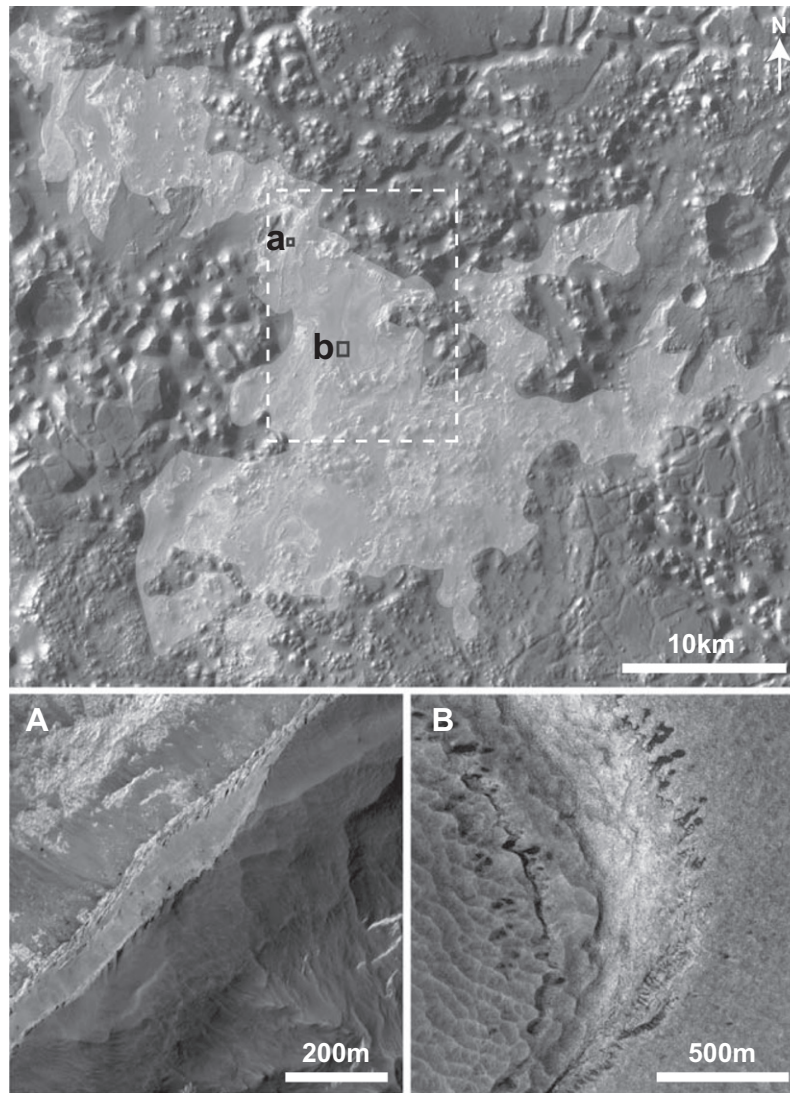
Fig. 6. ILD in region A: Top – Mosaic of HRSC nadir images H0912_0000_ND3, H0923_0000_ND3 and H0934_0000_ND3. Regions showing significant ILD outcrop are roughly enclosed by the shaded area. This boundary does not exclusively contain ILDs, nor does it cover all ILDs in the region, but it does provide a rough estimate of where there is significant light-toned material exposed at the surface. This is largely due to the heavily eroded nature and sporadic outcropping habit of ILDs in this region. The dotted white outline shows the area covered by Fig. 7. Bottom – (a) Portion of HiRISE red image PSP_009748_1785_RED showing a section of a cliff formed by a light-toned unit. (b) Portion of HiRISE image PSP_003907_1780_RED showing a contact between two moderate albedo, relatively flat units in the central topographic depression of region A.

~300–320 and ~0.14 for the surrounding hummocky terrain). Fig. 4 shows that our THEMIS-derived thermal inertias for ILDs in region A, range from ~500 tiu for portions of the flat embaying deposits to ~650–700 tiu for exposures of light-toned material on the slopes of chaotic mounds. This spread of values (as for all ILDs in Iani Chaos) could be due to varying degrees of dust coverage or could simply indicate that there are different classes of ILDs that are located at different stratigraphic positions. The discrepancy between TES and THEMIS thermal inertia values for ILDs is likely caused by spatial averaging that occurs within TES pixels due to their larger size ($\approx 3 \times 5$ km). TES pixel footprints include non-ILD material, which could work to lower the apparent TES thermal inertia if the non-ILD material has a lower thermal inertia than the ILD.

3.2. Region B

ILDs in region B are located towards the head of Ares Vallis (Figs. 1 and 2B). This area contains the lowest elevation topographic depressions in Iani Chaos, which lie 800 m below the start

of the main Ares Vallis channel. Warner et al. (2011) demonstrated, by analysis of cut-off flood grooves, that these basins formed as a result of subsidence after the major flooding events that carved Ares Vallis. ILD surfaces in region B lie above flood surfaces in proximal Ares Vallis (apart from one minor northern outlier) and were likely deposited after basin formation. This led Warner et al. (2009) to rule out a lacustrine origin for ILDs in this region since the low elevation of the entrance to Ares Vallis meant there was no northern barrier to cause ponding of floodwaters to the elevation required to produce the observed ILDs. Two main deposits are accompanied by smaller outcrops (Fig. 8), perhaps suggesting that the unit was once more expansive. The highly eroded nature of these ILDs suggests that they have been subject to a great deal of degradation.

The western-most formation, which we designate B1, is roughly 50×20 km in size with its longest dimension oriented approximately SW–NE. Erosional features trend SE–NW and mounds composed of darker material appear to be superposed atop the light-toned material. Yardangs are the dominant aeolian erosional feature and deposits of low albedo sand populate topographic
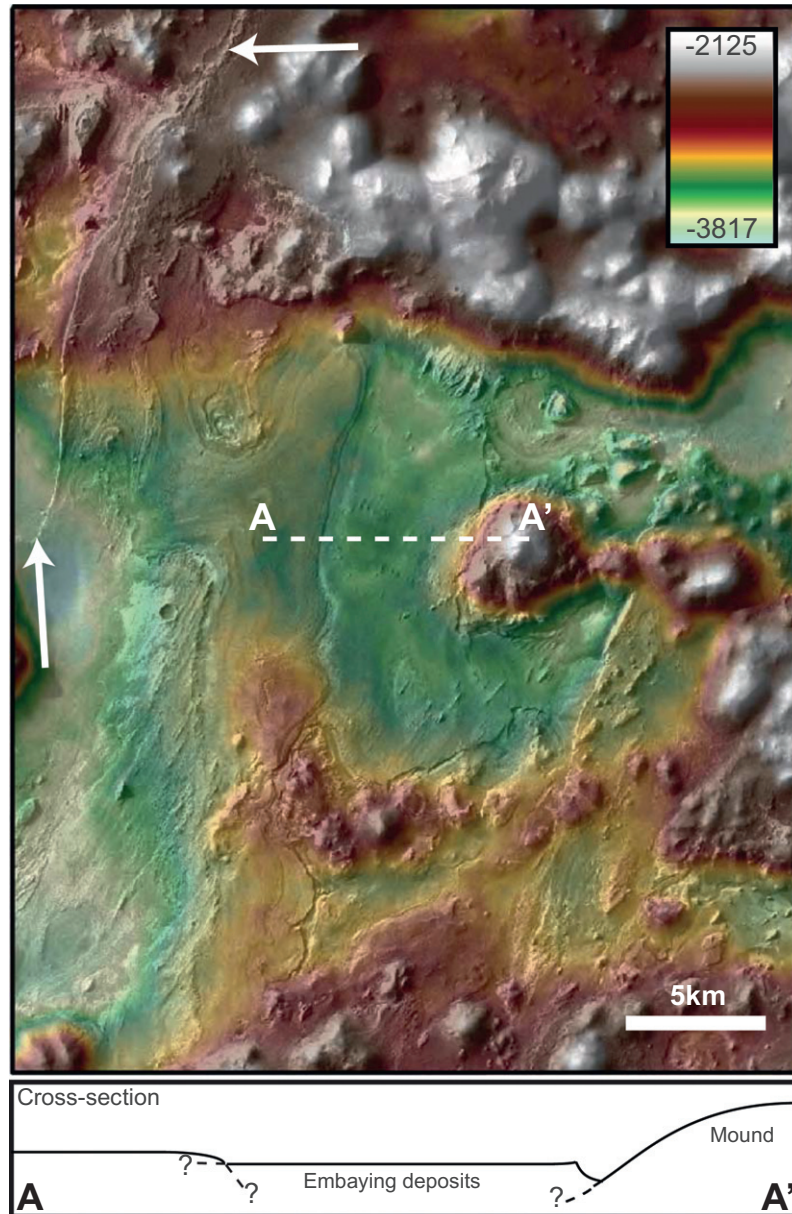
Fig. 7. ILDs in region A. Upper: Colourised stereo-derived topography from HRSC observation H0923_0000 superimposed on nadir channel data. The standard deviation of differences between HRSC DTMs and the 128 ppd MOLA elevation data is ∼50 m (Gwinner et al., 2010) and the MOLA DTM itself has an error of ±30 m (Zuber et al., 1992). White arrows indicate a cliff-forming unit composed of light-toned material that spans a wide elevation range. Lower: Geologic cross section (along white dashed line in upper panel) showing a plausible relationship between the overlying deposits and chaotic mound at A′.

depressions between them. Layering is also evident at the sub-decametre scale (Fig. 8a). The dominant orientation of erosional features is SE–NW, which corresponds to a 'trade-wind' direction (low-altitude tropical easterlies). However, small areas of the ILD surface show lineations oriented differently, which could imply aeolian modification of the ILD during epochs of different paleo-wind direction or, alternately, by winds variable in direction (e.g. daytime vs. nighttime, topographic forcing or seasonal variation) during the same epoch.

The eastern deposit, B2, lies at a generally lower elevation than B1 and appears to exhibit fewer linear erosion features than B1 (Fig. 8c). Best-fit thermal inertias derived for B1 approximately span the range 500–800 tiu, whereas those for B2 tend to be about 100 tiu lower, at 400–700 tiu (Figs. 4 and 5). Both deposits show a similar and relatively wide range of albedos, 0.15–0.30 (Fig. 5). Dark-toned, loose material trapped in grooves between yardangs

may be the cause of the wide thermal inertia–albedo distribution for deposit B1 shown in Fig. 5. The lower end of the distribution may be extended by the presence of this low albedo, low thermal inertia material, whose appearance and thermophysical properties match that of basaltic sand.

3.2.1. Topographic analysis

ILDs in this region are exposed at low elevations relative to the surrounding plateaus, but above the deepest parts of the basins in which they lie. ILDs in region B have a mean elevation of approximately −3,375 m, significantly lower than the mean elevations of ILDs in regions A (−2775 m), C (−2810 m) and D (−2740 m). In several locations in region B, aeolian deposition of sand or dust on contacts of ILDs with adjacent units can give the appearance that they emerge from beneath chaotic mounds or mesa slopes. However, this would imply that ILDs are older than the chaotic
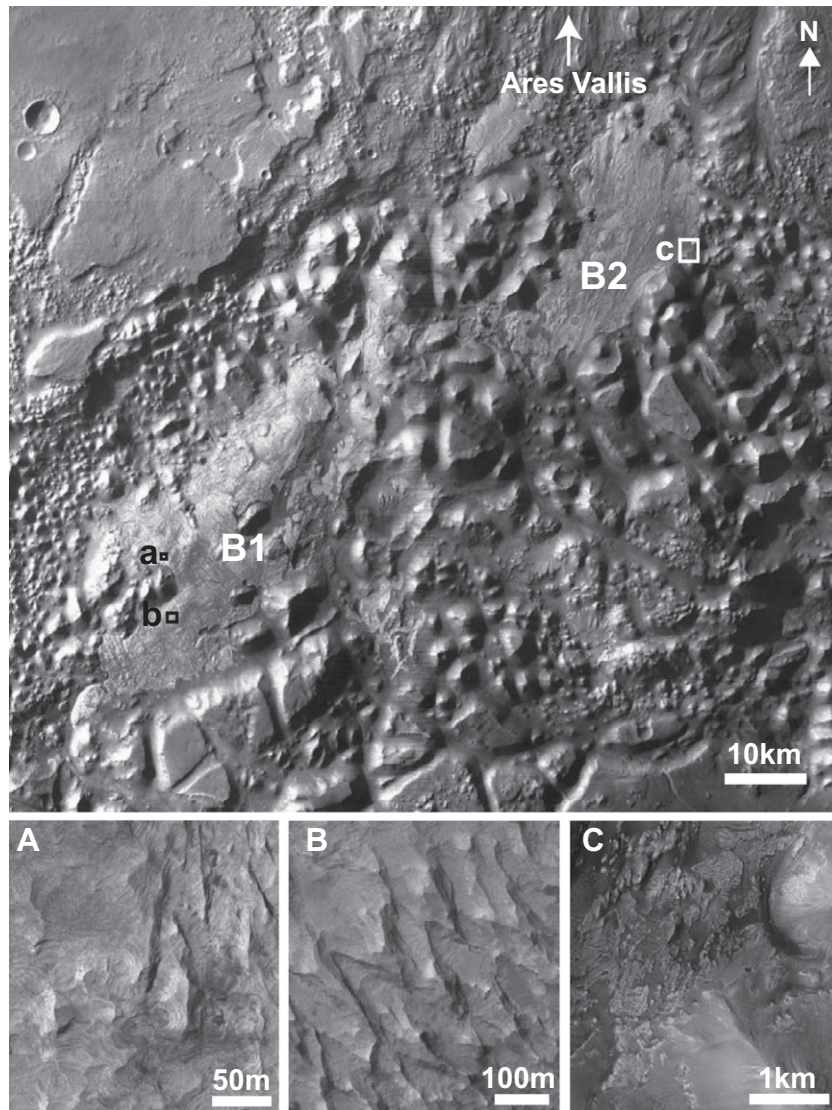
Fig. 8. Region B: Top – Mosaic composed of HRSC nadir data products H0923_0000_ND3 and H0934_0000_ND3 showing the context of ILDs in region B, which are overlaid with a shaded area. Two main ILDs are designated B1 and B2 and the locations of sub-frames a–c are marked by boxes. Bottom – (a) Portion of HiRISE image PSP_008100_1790_RED showing fine-scale layering on ILD B1. (b) Portion of HiRISE image PSP_008100_1790_RED showing aeolian fretting on ILD B1. (c) Portion of HiRISE image ESP_012293_1800_RED showing light-toned layered exposures outcropping at the base of chaotic mounds.

terrain, which might be unlikely since there is no evidence for dissection or erosion of ILDs by chaos forming processes such as fluvial incision and subsidence.
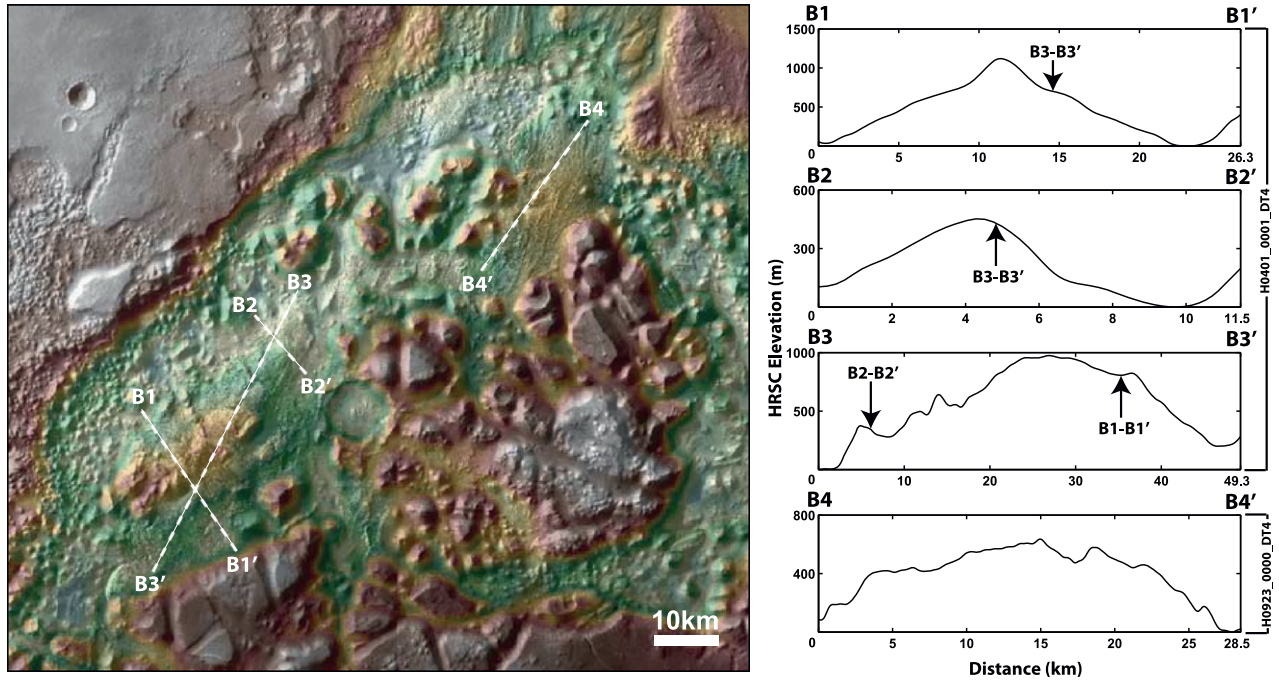
A dome-like morphology of the ILDs in region B is apparent and, notably, that of deposit B1 is particularly pronounced. Topographic transects of deposits B1 and B2 were extracted from HRSC stereo-derived data products (Fig. 9). The largest exposure, to the southwest of the region bears the most striking example of dome morphology along both its long (transect B3) and short (transects B1 and B2) axes. Underlying chaotic blocks could support the dome-like morphology. We are unable to determine if the internal stratigraphy is also domed, i.e. beds dip away from an axis. Anomalies in the dome-like nature of elevation profiles B1–B3 are due to chaotic mounds and erosional heterogeneities on ILD slopes. Transect B4 defines the footprint of a roughly NE–SW trending topographic profile of the ILD that lies closest to the head of Ares Vallis. The jagged nature of the elevation data is due to approximately S–N trending depressions and scour features, indicating significant erosion. The northern ILDs upper topographic limit peaks at a slightly lower

relative altitude of −2900 m compared to the larger ILD (represented by transects B1, B2 and B3), which peaks at −2850 m.
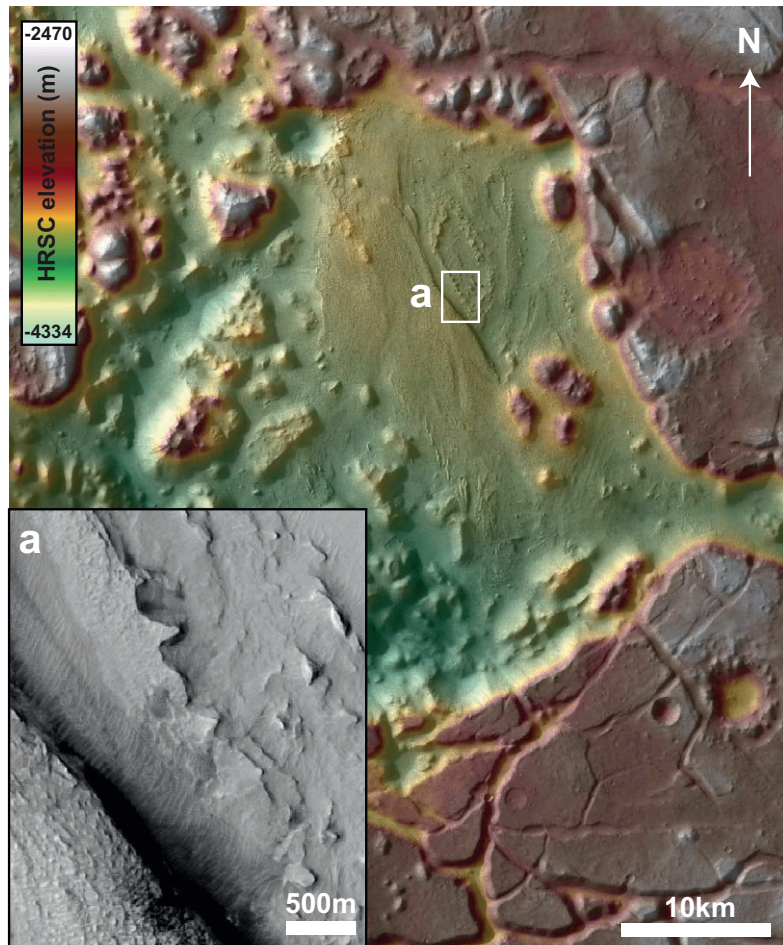
3.3. Region C

The ILD in region C appears to outcrop in a quasi-circular structure (Fig. 10). Its morphology suggests that of an ancient impact crater that was infilled, perhaps by volcanic or sedimentary deposits. ILDs are generally flat, but in places form cliffs and eroded remnants (Fig. 10a). THEMIS-derived thermal inertias of these deposits (shown in a MOC image: Fig. 10a) are average for ILDs in Iani Chaos (500–600 tiu), but derived albedos are generally higher (0.2–0.4, with a mean close to 0.34).

However, we remain cautious of interpreting this result to mean that region C has mineralogical or morphological differences to other ILDs, since THEMIS daytime apparent brightness temperatures (which derived albedo is predominantly controlled by) could have been adversely affected by the seasonal variation of dust aerosols (Section 2.2 and Table 1).

Fig. 9. Topographic profiles across the ILDs in region B showing a dome-like morphology, notably of the larger deposit to the southwest. Stereo-derived HRSC data products H0401_0001_DT4 (transects B1–3) and H0901_0000_DT4 (transect B4) were used in creating topographic profiles. The left panel base image is MOLA 128 pixel per degree topography overlaid on aligned HRSC nadir imagery from data products H0934_0000_ND3 and H0923_0000_ND3.

Fig. 10. Context of ILDs in region C. Stereo-derived topography from HRSC product H0901_0000_DT4 superimposed at 70% transparency on nadir image H0901_0000_ND4. (a) Portion of MOC-NA image E1700667 showing the area outlined by the white box in the left panel.
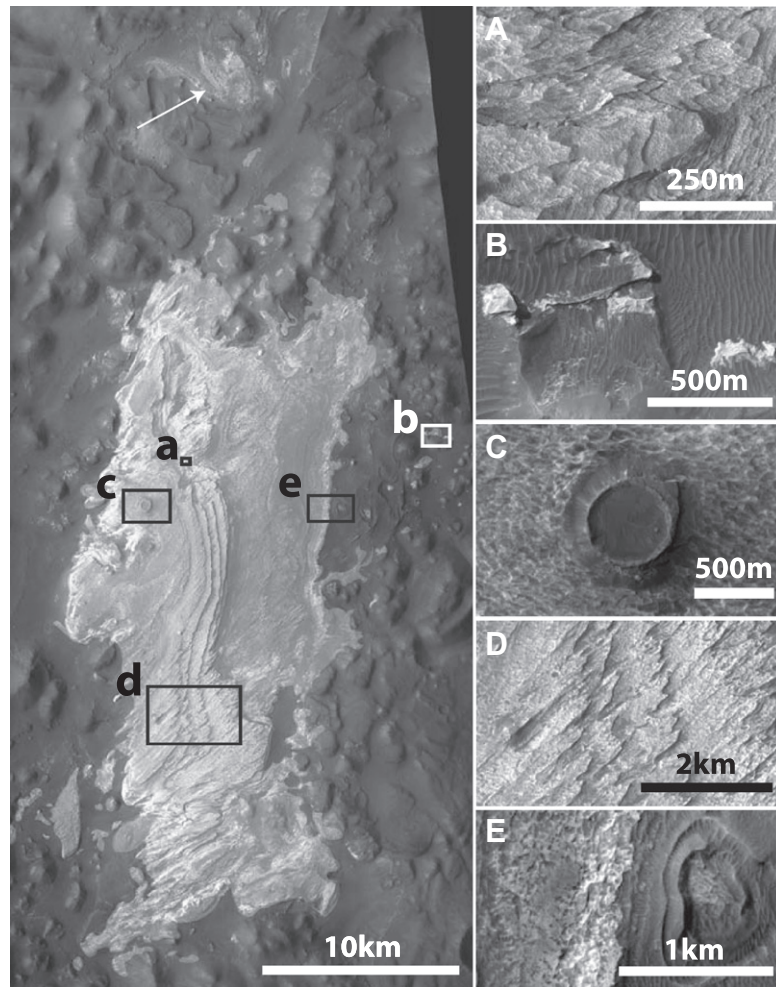
Fig. 11. Geologic context of ILDs in region D illustrated with monochromatic imagery. Left: CTX image P04_002628_1757 showing the locations of the expanded regions on the right. The white arrow indicates finely layered light-toned material exposed on south-facing slopes to the north of the main ILD. Right: (a) portion of HiRISE PSP_002628_1760_RED showing scalloped surface texture, fine-scale layering and sharp erosional features, (b) Portion of HiRISE image PSP_010236_1760_RED showing scattered light-toned outliers in a topographic basin to the east of the main formation, (c) Portion of MOC-NA image E0301845 showing a pedestal crater atop the main formation, (d) Portion of CTX image P04_002628_1757 showing heavily eroded bench-cliff structure with SW–NE aligned erosion features and aeolian fretting. (e) Portion of CTX image B02_010236_1758 showing pseudokarst terrain in low elevation layers.

The footprint of CRISM data product FRT0000848C is proximal to the ILD in region C but does not directly cover any exposed areas of it. In addition, the signal to noise ratio of the product is low throughout all bands and the data is of poor quality. The creation of spectral summary parameters and preliminary analysis of this cube yielded no spectral features of note.

3.4. Region D

The region is situated in the southernmost topographic depression in Iani Chaos and comprises one main ILD (Fig. 11, left panel) with outliers distributed in the surrounding terrain. The main formation appears as an elongate outcrop roughly 33×14 km with the long dimension in a N–S orientation. It shows intermediate to high albedo and is strikingly layered on a variety of scales (Fig. 11a). Pronounced bench-cliff structures on the eastern side of the formation indicate 10–20 m beds that are dipping to the southwest (Fig. 12, Profile D2–D2′). Towards the southern portion of the ILD the bench-cliff structures have been eroded to form sharp spurs with their long axes oriented in a SW–NE direction. The southern portion of this unit shows a lower surface elevation and more significant erosion of the ILD into elongate ridges.

Knobs and other exposures on the slopes of small mounds lie in a topographic basin to the immediate east (Fig. 11b). These represent the lowest elevation portions of the unit and are probably remnants or exposures of an eroded section that once extended to the east. Between these knobs and the bench-cliff structures lie thinner, stratigraphically low beds that are mantled with fine material. They show directional erosional features and some pseudokarst topography (Fig. 11e), perhaps indicative of dissolution of soluble minerals at low-elevations. They generally show lower thermal inertias than the main deposit ($\sim$400–500 tiu compared to $\sim$550–700 tiu). Lower apparent thermal inertias could be due to a lower density/degree of induration or due to a thin cover of low thermal inertia material.

A $\sim$520 m diameter pedestal crater, centred at 341.41°E–4.16°N lies atop the main ILD (Fig. 11c). The crater floor lies $\sim$105 m above the surrounding pitted surface of the ILD, suggesting extensive removal of the surrounding material since the crater's formation. The crater appears dark compared to deposit on which it is located, suggesting that its pedestal is composed either entirely of impact-hardened dark material (implying the light-toned deposit was once overlain by a thick cover of regolith) or light-toned layered material mantled by a layer of impact-hardened dark material.
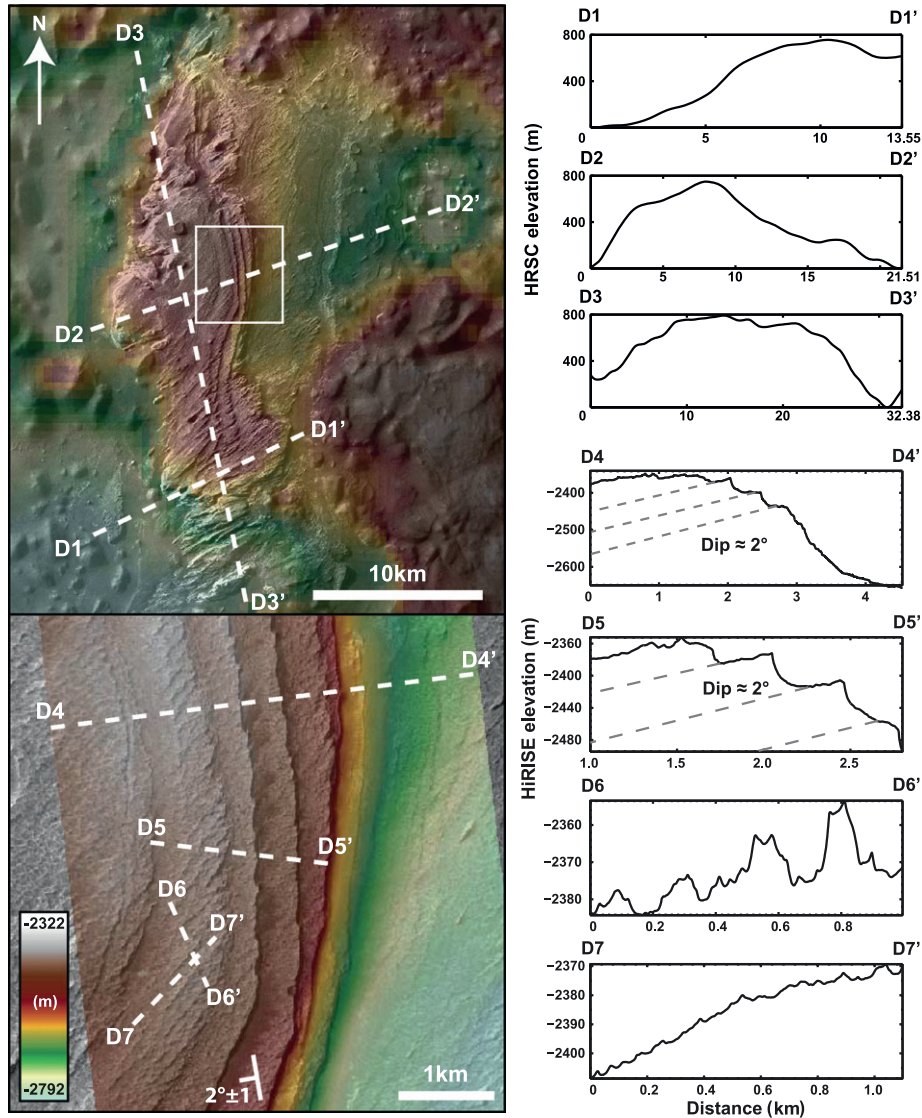
Fig. 12. Upper: Topographic profiles across the ILDs in region D extracted from stereo-derived HRSC data product H0401_0001_DT4 (175 m/pixel). The left panel base image is colourised MOLA 128 ppd topography overlaid on HRSC image H0934_0000_ND3. The white box outlines the area in the lower panel. Lower: HiRISE stereo-derived DEM created using products PSP_002206_1760 and PSP_002628_1760. Colourised HiRISE elevation is overlaid on CTX image P20_009036_1758. Topographic profiles D4–D8 are marked as white dashed lines: D4 – Full lateral transect of the eastern half of the ILD, D5 – Detail of bench-cliff structure, D6 – Transverse profile of erosional features on upper bench and D7 – Profile along erosional valley on upper bench. For profiles D4 and D5, grey dashed lines represent plausible layer boundaries within the unit. A dip and strike symbol represents the result of fitting a plane to 12 points selected on a bench. (For interpretation of the references to colour in this figure legend, the reader is referred to the web version of this article.)

Aeolian fretting tends to occur on the eastern sides of the ILD in the cliff-forming units (Fig. 11d) and its orientation would suggest erosion in a SW–NE direction.

Aeolian fretting may be described as wind removal of grains from aggregate material leaving behind erosion-resistant formations. Its effects on Earth are seen in cemented sand dunes (Thomas et al., 2005). Aeolian fretting is not related to 'fretted terrain', a broader scale erosional phenomenon meaning smooth, flat lowland areas separated from a cratered upland by abrupt escarpments (Sharp, 1973; Carr, 2001).

The orientation of the long axis of these features could represent a SW–NE prevailing wind direction, perhaps channelled by valley sides. The prevalence of aeolian modification features such as aeolian fretting, yardangs and deflation pits suggests the primary cause for the surface texture of ILDs in region D is sustained aeolian modification during the Amazonian, which is consistent with a crater retention age of ∼22 Ma calculated by Warner et al. (2011).

To the north of the region, finely layered beds are exposed on south-facing slopes (marked by a white arrow in the left panel of Fig. 11) that show the same scalloped surface as the top of the main formation, suggesting a similar erosional regime. Their exposure on and at the base of slopes could indicate that they extend beneath the surrounding landscape, which is of higher elevation than the main deposit and only partially degraded into chaotic terrain.

ILD surfaces generally show a scalloped surface texture at the scale of a few metres, similar to intermediate-toned units in Aram Chaos that were found to be rich in haematite (Glotch and Rogers, 2007). Using spectra from ESA's Observatoire pour la Minéralogie, l'Eau, les Glaces et l'Activité (OMEGA), Gendrin et al. (2005) found the ILDs in region D to show a strong gypsum spectral signature and we confirm this in our analysis of CRISM data (see Section 4). Thermal inertias of the main ILD lie in the range 400–700 tiu (Figs. 4 and 5) although the presence of dust or sand in topographic depressions that are smaller in size than a THEMIS pixel (∼100 × 100 m) may be causing a reduced lower bound compared

to the true value for the ILD. Derived albedos tend to be representative of the average for ILDs in Iani Chaos, about 0.20–0.35.

3.4.1. Topographic analysis

The main ILD in region D is covered by the footprints of three independent topographic datasets: MOLA, an HRSC stereo-derived digital elevation model (DEM), and a HiRISE DEM. The MOLA 128 ppd topography is used as the colourised base map in Fig. 12. The HRSC DEM is at 175 m/pixel and available from data product H0401_0001_DT4. Linear elevation profiles D1–D3 are extracted from the HRSC DEM.

The dome-like topographic profiles highlight the indurated nature of ILDs relative to the surrounding terrain, which is also reflected in their generally higher thermal inertias. MOLA data is not of sufficient resolution to accurately resolve bed dip. A dip direction away from the centre of the ILD would suggest a dome-like morphology, which could indicate tectonic modification of the unit by salt-diapirism during burial. However, using MOLA data alone, we see only that the formations erosion into a bench-cliff structure approximates a dome-shape, but that individual strata show no measurable dip.

At region D overlapping HiRISE images were used to create a HiRISE stereo-derived DEM. Using HiRISE products PSP_002206_1760 and PSP_002628_1760 a DEM and orthoimage were produced using the geospatial analysis software package SOCET SET® and the method of Kirk et al. (2008). Using the method of Okubo (2010), we estimate the vertical precision of our HiRISE DEM, assuming 1/5 pixel correlations, as 0.21 m. The ~1 m/pixel HiRISE DEM allows surface details such as small-scale erosional features and bench-cliff structures to be resolved. Elevation transects shown in Fig. 12 highlight several distinctive features of the morphology of ILD D.

Measurement of dip direction was made difficult by non-planar representation of the bench surfaces in the DEM, but the orientation of transect D5 (Fig. 12) represents our estimate of the average direction of dip for the benches. Extracting topographic profiles along transects D4 and D5 we estimate bench dip at about 2°, ignoring areas with accumulations of darker material at the base of cliffs (where thermal inertia was ~400–500 tiu, suggesting very coarse sand or perhaps indurated material). We verify this estimate by selecting locations on a bench we believe to be the best-exposed bed surface and best-fitting a plane using the method of Fueten et al. (2005, 2008) and Okubo (2010). The orientation of a plane with 99.69% goodness of fit to the points strikes at 170.4 ± 10.5° and has a dip of 2 ± 1° (Fig. 12), agreeing well with our wider estimate for all benches in the HiRISE DEM.

If the bench-surfaces are proxies for bed-surfaces then the eastern side of the ILD does not show evidence for central doming of ILD D, since dip would need to be in an opposite sense in order for the centre to exhibit a central stratigraphic elevation. However, were this unit to be sedimentary and thus deposited in an approximately flat environment, any dip could reflect tectonic modification of the unit after its emplacement upon pre-existing

topography. This would be in agreement with Warner et al. (2011), who suggest that collapse in Iani Chaos may have occurred in multiple stages and extended into the Amazonian.

Sowe (2009) measure the dip of bench-forming beds in the opposite direction, supporting a dome-like morphology for ILD D. However, those conclusions were drawn using stereo-derived topography HRSC DEM displayed in Fig. 12, which does not resolve the dip of individual beds on the eastern flanks. The abrupt termination of the cliff-forming beds could suggest they once extended farther to the east. More extensive subordinate strata that are superposed by the cliff-forming units as well as small ILDs scattered in the topographic depression ~10 km to the east could be remnants of this once larger unit.

4. Analysis of CRISM spectra

Spectral features exhibited by ILDs in Iani Chaos are indicative of sulphates. Mg^{2+} was first predicted to be the predominant cation associated with the sulphate ion on the surface of Mars (Clark and Van Hart, 1981), while Fe, Na, K and Ca sulphates were predicted to be present in lesser amounts. OMEGA-derived signatures indicating the presence of gypsum were reported on the upper beds of the ILD in region D (Gendrin et al., 2005). An absorption at 1.96 μm observed in CRISM spectra supports the presence of gypsum and kieserite (Noe Dobrea et al., 2006). Bibring et al. (2007) note that while ferric oxides are often coupled with sulphate spectral signatures, this is not the case for the main ILD in region D. However, Niles and Michalski (2009) report that haematite that occurs with sulphates in Iani Chaos and Auruem Chaos has the same spectral signature of that found in Terra Meridiani, where in situ observations by NASA's Opportunity Rover led to the discovery of haematitic concretions, nicknamed 'blueberries' (Squyres et al., 2004a,b). This may indicate episodic diagenesis in Iani Chaos during periods of groundwater saturation.

The formation of the Ares Vallis outflow channel is thought to have occurred in multiple stages (Warner et al., 2009), which necessitates recharge of the subsurface in its primary source region, Iani Chaos (Harrison and Grimm, 2008).

Groundwater saturation events have been suggested to be initiated by climatic forcing, impacts or increase of the geothermal gradient by proximal magmatism.

Through analysis of CRISM spectral summary parameters and individual absorptions we find strong evidence for the presence of a variety of poly- and monohydrated sulphates. We also address issues pertaining to the validity of detected absorptions, which may be affected when characteristic spectral features are altered by prolonged exposure to martian surface conditions (Cloutis et al., 2008; Dalton et al., 2011).

4.1. Method

CRISM full-resolution targeted data records (TRDRs) were acquired from the PDS and processed to correct for artefacts caused

Table 2
Details of CRISM spectral summary parameters used in this study, as derived by Pelkey et al. (2007) CRISM band identifiers comprise an 'R' (radiance) followed by the approximate central wavelength of the band in nanometres e.g. R2120 is the spectral radiance, $\Re$, at 2.12 μm. 'CR' represents continuum-corrected radiance.[a]

Name	Parameter	Formulation [a]	Rationale
BD1900	1.9 μm band depth	$1 - (((R1930 + R1985) \times 0.5)/(a \times R1857 + b \times R2067))$	H_2O
BD2100	2.1 μm band depth	$1 - (((R2120 + R2140) \times 0.5)/(a \times R1930 + b \times R2250))$	Monohydrated minerals
SINDEX	2.4 μm drop	$1 - ((CR2390 + CR2430)/(CR2290 + CR2320))$ (CR values are observed R values divided by values fit along the slope as determined between 1.8 and 2.53 μm.)	Hydrated minerals; particularly sulphates

[a] The letters a and b in band depth formulations represent fractional distances between wavelengths; for example, given BD_C, a band depth at a central wavelength C with nearby continuum points defined at shorter and longer wavelengths S and L: $BD_C = 1 - R_C/(a R_S + b R_L)$, where $a = 1 - b$ and $b = (\lambda_C - \lambda_S)/(\lambda_L - \lambda_S)$.
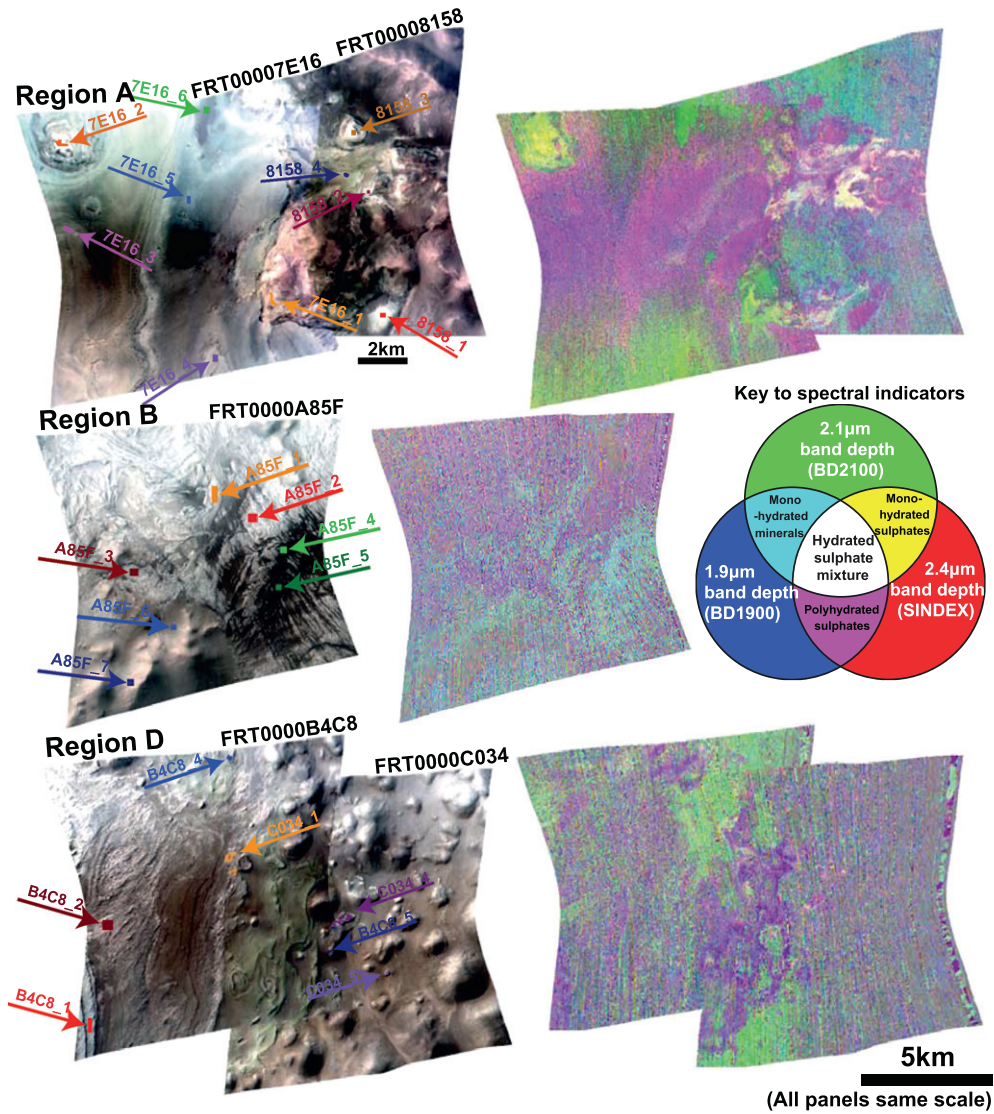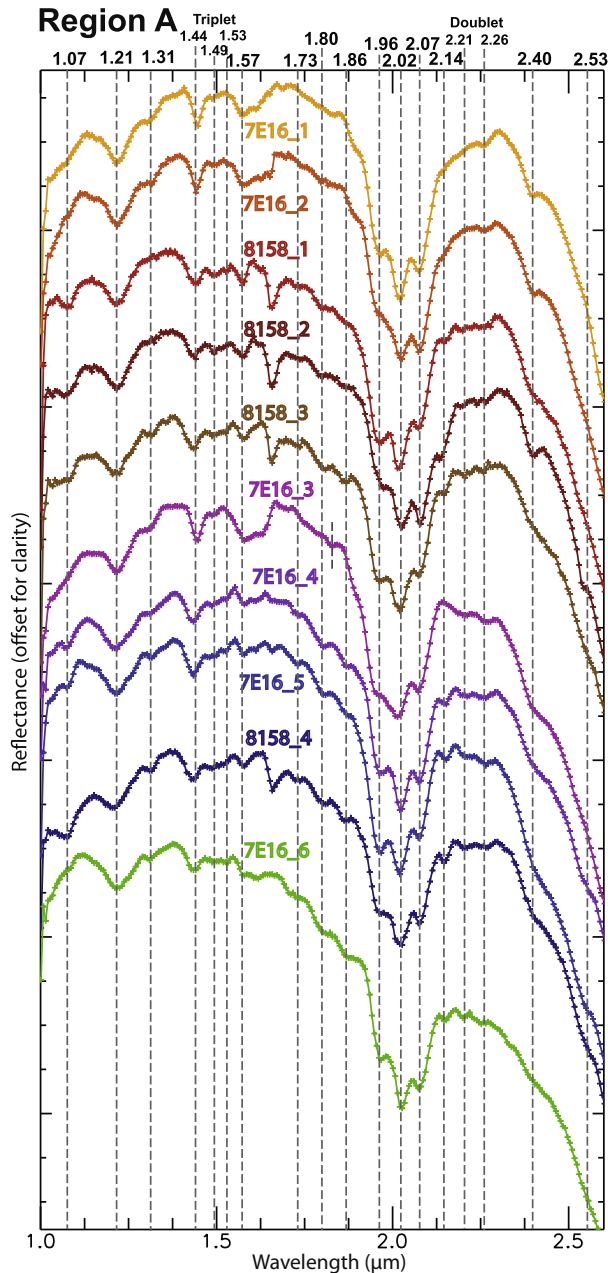
Fig. 13. Summary plots for the CRISM data products used in this study. Cubes in mapping areas A (7E16 and 8158), B (A85F) and D (B4C8 and C034) are shown. Left – False colour images using CRISM bands centred at 2.5361 μm, 1.5132 μm and 1.0865 μm for red, green and blue channels, respectively. Right – RGB composites using three key summary parameters from Pelkey et al. (2007) that are relevant to the mineralogy of ILDs: Red – 2.4 μm band depth (sulphate minerals), Green – 2.1 μm band depth (associated with monohydrated minerals) and Blue – 1.9 μm band depth (stronger in polyhydrated sulphates than in monohydrated sulphates). Location and extent of regions of interest, from which spectra were extracted and averaged are labelled by arrows. (For interpretation of the references to colour in this figure legend, the reader is referred to the web version of this article.)

by atmospheric absorption, striping and noise (Morgan, 2009). We completed these steps using the CRISM analysis toolkit (CAT) v6.7. The CRISM instrument contains visible/NIR (0.36–1.07 μm) and infrared (1.0–4.0 μm) detectors. Infrared TRDRs containing I/F (incidence/solar flux at 1 AU) values were corrected for atmospheric absorption using the 'volcano-scan' method. Visible/near-infrared (VNIR) wavelength spectral cubes did not require this step, since the martian atmosphere is transparent in this spectral range. Isolated noise spikes were filtered from IR wavelength cubes and both VNIR and IR cubes were passed through a destriping algorithm. Spectral summary parameters defined by Pelkey et al. (2007) were derived in order to show relative strengths of characteristic spectral features (see Table 2 for parameters selected for use in this study). Spectral summary parameters were 'flattened' to remove banding along lines (i.e. the N–S direction) and to correct for spectral 'smile', an artefact common to push-broom sensors caused by the dependance of central wavelength and spectral resolution on across-track position. Finally, spectral cubes

and summary parameters were map-projected using latitude and longitude information contained in their associated derived data records (DDRs).

We plot Red–Green–Blue (RGB) composite images using selected CRISM spectral summary parameters (Table 2) to illustrate the apparent distribution of hydration and sulphate features in ILDs in Iani Chaos. Specifically, we focus on band depth at 1.9 μm (known as BD1900), band depth at 2.1 μm (BD2100) and a drop in reflectance at 2.4 μm (SINDEX), which are reported to indicate the presence of bound H_2O, monohydrated minerals and hydrated sulphates, respectively (Pelkey et al., 2007). Representing these parameters as the red green and blue channels of a composite image allows direct correlation of spectral trends with textural, stratigraphic and thermal properties derived from other geo-referenced data. CRISM products FRT0000-A85F, -7E16, -8158, -B4C8 and -C034 were selected for use in this study due to their interesting spectral signatures and good coverage of interior layered deposits. Product 848C, while presented in Fig. 13, was excluded from

Fig. 14. Spectra extracted from CRISM cubes 8158 and 7E16 for analysis of mineralogy in region A.

but small enough to represent geologic materials that were mineralogically and texturally homogenous over the region of selected pixels. Typically, ROIs comprised between 50 and 250 pixels. Ideally, spectra may be ratioed with a spectrally bland region in the same range of line numbers to eliminate the effects of spectral smile and instrument artefacts (Morgan, 2009). However, we found the lack of spectrally uninteresting regions in the areas covered by the CRISM cubes available for Iani Chaos to cause the act of ratioing spectra to produce false absorptions where none were present and sometimes to cancel out absorptions that are present. We note a similar problem was encountered by Bishop et al. (2009) and adopt their strategy by using only unratioed spectra to characterise phases that may be present in the ILDs in Iani Chaos.

Most hydrated sulphate minerals show several absorptions in the 2.0–2.7 μm wavelength range that are attributed to combinations of H_2O or OH bending, stretching and rotational fundamentals or S–O bending overtones (Cloutis et al., 2008). In our averaged spectra, superposition of these absorptions due to mixing of phases below the spatial resolution of CRISM causes this spectral domain to often become peppered with ambiguous absorptions. Therefore, we take great care in suggesting candidate phases when assigning a mineral to a spectral unit by ensuring the characteristics of the spectra are unique.

Spectral summary parameters were created for each of the CRISM data products used in this study and are plotted in RGB space in Fig. 13. In addition, false colour representations of the footprint are plotted using CRISM bands centred at 2.5361 μm, 1.5132 μm and 1.0865 μm. Immediately it is clear that the 1.9 μm spectral signature associated with polyhydrated sulphates are relatively common, while units likely to contain a greater proportion of monohydrated minerals are present but less extensive.
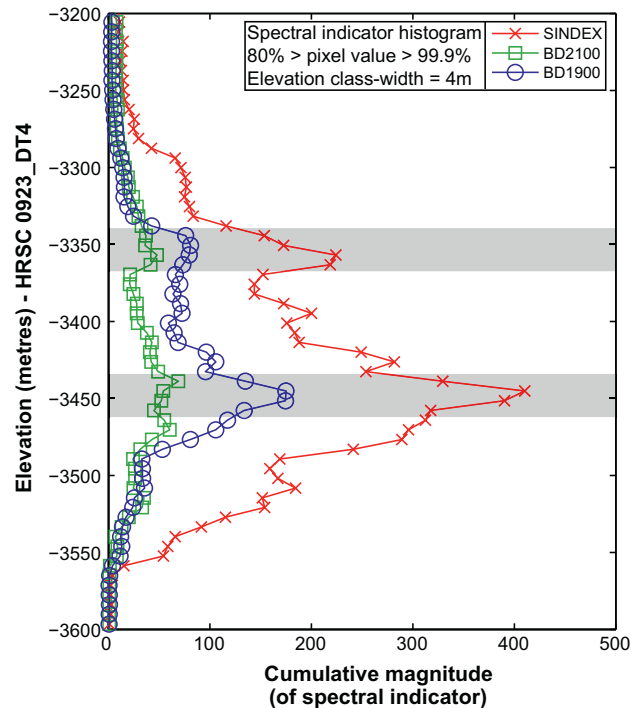
Fig. 15. Spectral summary parameter intensity vs. elevation for CRISM cubes 7E16 and 8158. The pixels used for these plots are those that lie between the 80th and 99.9th percentile of each band's distribution. This approach eliminates background noise near the mean and high-level spikes, which reveals signatures from rock units that show strong spectral features. Elevation class widths are 4 m. The value in each class (the data points) is the cumulative weight of the spectral summary parameter pixels in that elevation range. Shaded areas reveal two elevation ranges subject to higher concentrations of sulphate and hydrated minerals.

detailed analysis due to poor signal-to-noise ratio, few spectral features of interest, and an inappropriate footprint.

A narrow apparent absorption centred at 1.65 μm that varies in depth between CRISM cubes is an instrumental artefact (Farrand et al., 2009) and is therefore ignored. A second and wider apparent absorption that surrounds 2.0 μm is introduced by the volcano-scan method of atmospheric correction (Morgan, 2009). Knowledge of these characteristics, introduced by the instrument and processing-pipeline, negates misinterpretation of spectral features at those wavelengths.

Spectral summary parameter maps were used in conjunction with monochromatic images from other datasets to select regions of interest (ROIs) for further spectral analysis. To simplify spectral unit identification it is preferable to ensure that the minimum number of phases is represented by extracted spectra. ROIs over which spectra were averaged, were large enough to reduce noise,

Product FRT00008158 shows several white areas, suggesting rock type that exhibits the spectral characteristics of a hydrated sulphate mixture with mono and polyhydrated phases. Two main classes of light-toned layered deposits are identified in CRISM products FRT0000B4C8 and FRT0000C034: polyhydrated (purple) and monohydrated (green) sulphate units.

4.2. Spectra in region A

The spectral summary map for central region A (Fig. 13) shows strong 2.1 µm and 2.4 µm absorptions (yellow) on the side of a chaotic mound centred at 342.50°E, 2.08°S and also in exposed layers within a pseudo-circular depression centred at 342.50°E, 1.98°S (Fig. 13). Regions coloured white, indicating a mixture of mono- and polyhydrated sulphate minerals, represent a high albedo, layered unit that is exposed on several hillsides and in layered terrains in flatter areas.

Averaged reflectance spectra for each region of interest are plotted in Fig. 14. Spectrum 7E16_3 (182 pixels) represents the highest elevation embaying bed of the ILD (see Fig. 13) while 7E16_5 (144 pixels) represents a stratigraphically lower bed of the same formation. 7E16_4 (196 pixels) is taken from a slightly raised and higher albedo portion of a lower bed. To the northwest a curious quasi-circular erosional feature exposes light-toned beds in its interior and shows a strong mono-hydration signature (Fig. 13). Spectrum 7E16_2 (242 pixels) represents the average spectrum from pixels with the strongest mono-hydration signals in this feature.

Spectrum 7E16_6 (240 pixels) represents a dune-forming sand deposit. The terrain to the east of the embaying units shows exposed bright layers in jumbled terrain. A chaotic mound with slopes peppered with bright light-toned material rises some ~780 m above the surrounding plains. Spectrum 7E16_1 (219 pixels) represents an area on the slope centred at roughly 150 m above the plains that shows strong mono-hydration signatures (Fig. 13). Spectra 8158_4 (131 pixels) and 8158_3 (100 pixels) are from lower and upper stratigraphic positions, respectively, in the ILD that embays the chaotic mound. Spectrum 8158_2 (36 pixels) represents the side of a small eroded chaotic knob and spectrum 8158_1 (108 pixels) covers a ~0.8 × 1.5 km long exposure of bright ILD protruding from dark dunes in a topographic low that shows a strong polyhydrated sulphate signature.

4.2.1. Elevation mapping of spectral summary parameters

In order to constrain the altitude (and stratigraphy) of the major hydrated and sulphate-rich units in central Iani Chaos, we extract pixels from the spectral summary parameters BD1900, BD2100 and SINDEX where the pixel intensities lie between percentile-based limits. A lower limit of the 80th percentile allows distinction of beds of high-hydrated or sulphate content from background noise and an upper limit of the 99.9th percentile excludes high-level data noise (data in the top 0.1th percentile is very unlikely to be physically real and is probably noise). The extracted pixels are then geographically correlated to their HRSC elevation from H0923_0000_DT4 and the resulting spectral summary parame-
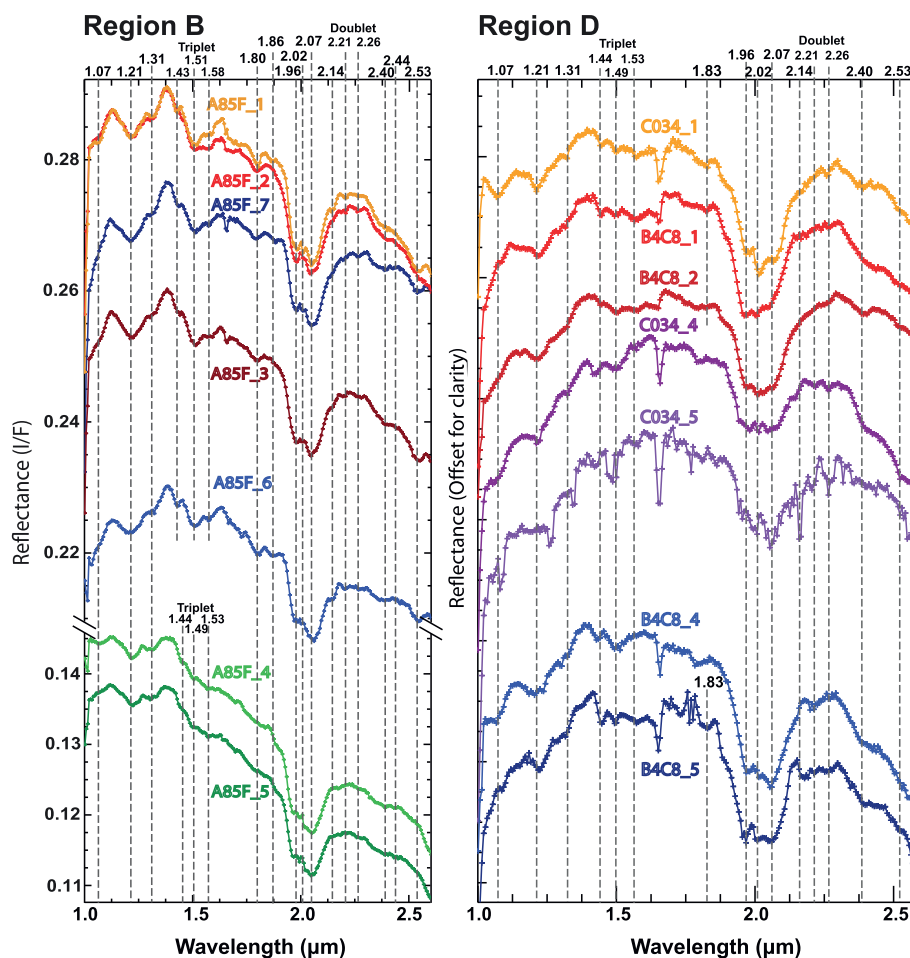

Fig. 16. Left: Spectra extracted from CRISM cube A85F for analysis of mineralogy in region B. Right: Spectra extracted from CRISM cubes C034 and B4C8 for analysis of mineralogy in region D.

ter–elevation data pairs are plotted in Fig. 15. Distributions are plotted as histograms with elevation classes that are 4 m wide.

Two major spikes in all spectral summary parameters are centred at −3350 m (small) and −3450 m (large) (Fig. 15). The lower altitude stronger spectral signatures suggest a more hydrated/ more evaporite rich unit that likely corresponds to the polyhydrated sulphate (purple) signatures on the flat embaying beds and exposed layers that surround the base of the chaotic mound. The smaller spike represents a less hydrated or less abundant set of exposures centred on roughly −3350 m. This spike likely represents the monohydrated (green) beds and scattered exposures on the side of the chaotic mound, as well as the layers that are concentrically exposed in the erosional feature to the north-west of the region (Fig. 13, spectrum 7E16_2). ILDs on older, protruding chaotic mounds show a lower state of hydration, while the younger embaying deposits show more polyhydrated sulphates. This observation could suggest either that older hydrated minerals have had more time exposed to the desiccating martian surface environment or that their environment of formation was not as wet as was the case for the younger deposits. Another possibility is that after chaos formation, subsequent aqueous episodes resulting from regional groundwater saturation would not have reached the upper chaotic mounds causing evaporite formation in only stratigraphically low units. Low-elevation ILDs would have therefore been more likely to experience later stage aqueous recharge. In general, spectra from region A show many similarities, however spectra from the lower-albedo, embaying deposits tend to show less pronounced absorption features, suggesting either reduced abundances of minerals, assemblages that are more desiccated through exposure to martian surface conditions or simply the obscuring of the unit surface by spectrally bland dust or sand.

4.3. Spectra in region B

For ILD B1 we define seven regions of interest for CRISM cube FRT000A85F (Fig. 16) that represent the three geologic units in the cube's footprint: the ILD, the eroded mounds and the dark material covering the ILD. Averaged spectra representing ILD B1 (Fig. 16) are A85F_1 (532 pixels) and A85F_2 (440 pixels). These two spectra represent portions of the ILD that are of the most typical type in this region; those with an eroded, scalloped surface texture and a predominantly ∼SE–NW orientation of erosional features (Fig. 13). Spectrum A85F_3 (357 pixels) represents a portion of the ILD that appears less eroded and that lies near the base of the hills in the SW of the cubes footprint. Spectra A85F_4 (288 pixels) and A85F_5 (195 pixels) represent the dark, wind-blown sand/dust mantling material that fills topographic cavities in ILD B1 and sometimes forms sheets with transverse dunes. Finally, two spectra were taken of the slopes of the mounds to the south west of the area (Fig. 13): A85F_6 (169 pixels) and A85F_7 (240 pixels).

4.4. Spectra in region D

Spectra representing the main ILD in region D are: C034_1 (345 pixels) from a stratigraphically low exposure to the east of the stepped ILD, B4C8_1 (320 pixels) from atop the lowest altitude bench on the stepped ILD and B4C8_2 (483 pixels) from the base of an eroded slope that appears to cut through the stepped structure (Fig. 13). Blocks composed of high-albedo material lie amongst dune fields and scattered knobs to the immediate east of the main ILD formation (Fig. 11b). Spectral summary parameters suggest a hydrated sulphate mixture similar to the main ILD (Fig. 13). Spectra were extracted and averaged for three areas of blocks/exposures and the resulting spectra are plotted in Fig. 16 as C034_4 (414 pixels), C034_5 (41 pixels) and B4C8_5 (166 pixels). The high level of noise in spectrum C034_5 is attributed to

the small number of pixels available to represent for the small blocky unit. B4C8_4 (120 pixels) represents a small (∼500 × 250 m) elevated mound protruding amidst several exposed layers that form a sub-circular feature, centred at 341.570°E, 4.006°S.

4.5. Common diagnostic absorptions

An absorption at 1.07 μm is most prominent in some stratigraphically low units in region A such as the eastern low-lying ILDs (spectra 8158_1, 2, 3 and 4) and some embaying ILDs (spectra 7E16_4 and 5). Only one relatively weak instance of this absorption is present in spectra of region B: Spectra A85F_4 represents dark material deposited atop the main ILD. In region D this feature is particularly pronounced in spectra of the outcropping lower strata of the main ILD (C034_1) and moderately pronounced in spectra of scattered light-toned outliers to the east (C034_4, C034_5, B4C8_4 and B4C8_5).

A strong absorption is observed at 1.21 μm in all spectra from regions A and D. In region B this absorption is strong in spectra representing ILDs (A85F_1, 2 and 3), moderately pronounced on chaotic slopes (spectra A85F_6 and 7) and is weakly present on superposing dark material (spectra A85F_4 and 5). An absorption of this approximate width and band depth is expected of gypsum, according to Clark et al. (1990) and Massé et al. (2010) and spectral libraries F1CC16B and LASF41A supplied by the NASA/Keck Reflectance Experiment Laboratory (RELAB). No other sulphate minerals that showed absorptions on or near this position were found in spectral libraries, with the exception of anhydrite (although anhydrite's 1.21 μm absorption is far shallower and therefore less likely to be prominent in un-ratioed spectra). However, Massé et al. (2010) also attribute an absorption at this position to the presence of water–ice (although this is likely to be an aerosol since the presence of equatorial surface water–ice is unlikely). CO_2 also has a minor absorption at this wavelength (Burch et al., 1968) and could be the cause if the atmospheric correction was not fully effective.

A weak absorption around 1.31 μm in almost all spectra in region A. In region B it is most pronounced on the ILD and slopes of the chaotic mounds. In region D the feature is similarly shallow and present in spectra of the outliers (B4C8_4 and 5) and of a bench of the main ILD (B4C8_1). Feature strength is variable and independent of column position in unprojected cubes ruling out an instrumental origin. Both water ice and CO_2 ice show absorptions at this location (Pelkey et al., 2007), however variation throughout the scene does not favour an atmospheric cause and surface ice is unlikely given the equatorial latitude. Alunite shows a small absorption here, but it may be too weak (Fig. 17) to be detected in unratioed spectra.

The spectral region between 1.4 and 1.6 μm shows several small absorptions, which could be attributed to several phases. A moderate absorption at 1.44 μm is accompanied by weaker features at 1.49 μm and 1.53 μm in all spectra. This triplet is characteristic of gypsum and in region A is strongest in spectrum 8158_1, an unusually high albedo exposure of ILD located on the SE base of the chaotic mound. We also note that jarosite shows an absorption at 1.48 μm. In region B we observe the triplet in a weak capacity and only in spectra of the dark material (spectra A85F_4 and 5). However, we observe the triplet in slightly shifted positions, 1.43, 1.51 and 1.57 μm, in spectra of the ILD and slopes of the superposed chaotic mounds (A85F_1, 2 and 3). The 1.57 μm absorption is much weaker than the previous two of the triplet, suggesting either that it is an up-wavelength shifted band of the triplet, or that it may represent a different phase. In region D, the triplet is present in virtually all spectra.

An absorption at 1.57 μm is exhibited in all spectra in region A, which suggests either that it is a data artefact or that it is produced
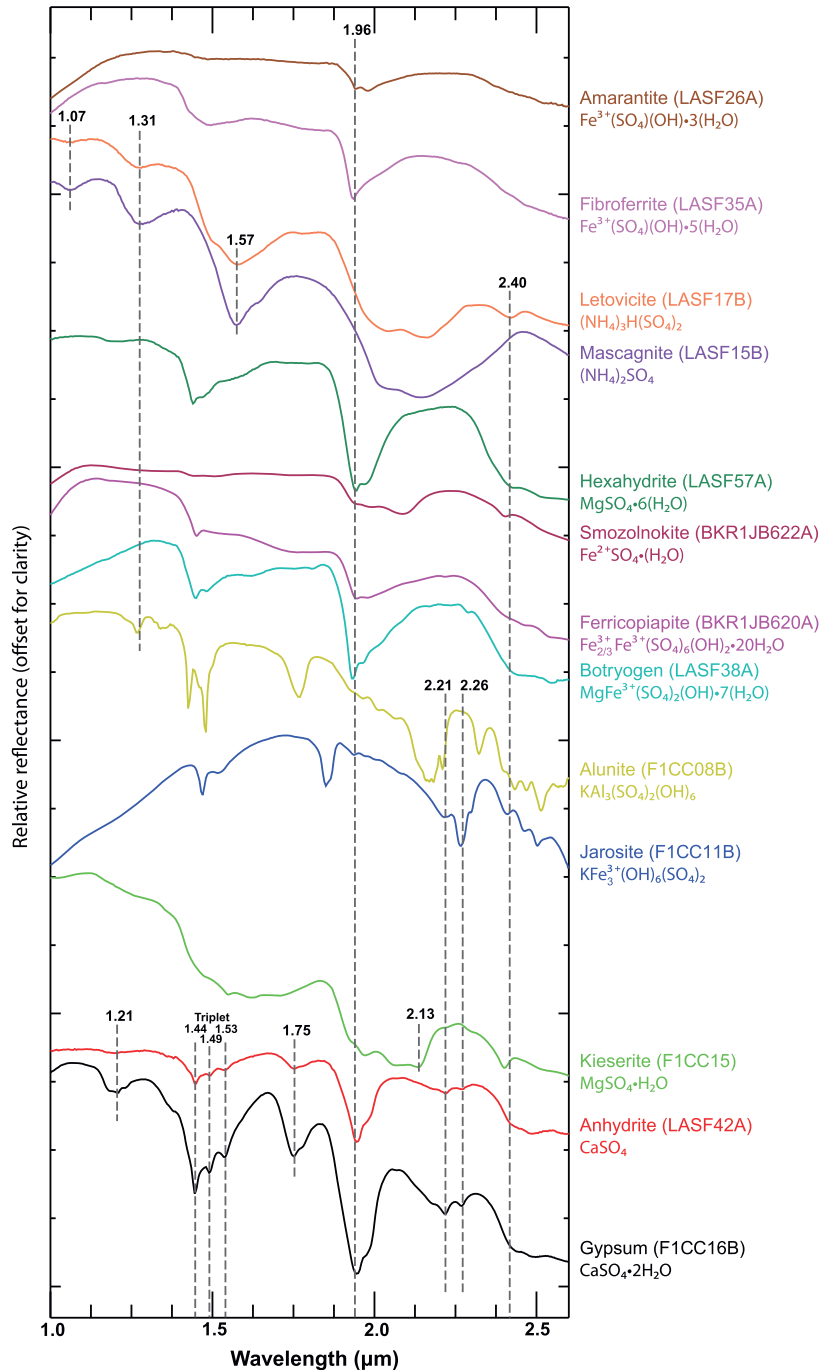
Fig. 17. Selected spectra plotted from RELAB libraries (catalogue numbers in brackets). Key absorptions on ILDs in Iani Chaos are indicated.

by a phase that is ubiquitous in this region (more likely since it is present in both CRISM products 7E16 and 8158).

In region A absorptions at 1.73, 1.80 and 1.86 μm are produced mainly by ILDs in eroded terrain to the east (spectra 8158_2, 3 and 4) but also by a bright surfaces exposed to the south of the chaotic mound (spectrum 7E16_4) and by the dune-forming dark material (spectrum 7E16_6).

An absorption at around 1.80 μm is commensurate with weak bands expected from gypsum, amarantite, ferricopiapite, copiapite and fibroferrite, while a strong absorption at this wavelength can also be produced by alunite (Cloutis et al., 2006). The spectrum of alunite is shown by Cloutis et al. (2008) to be largely unaltered by exposure to simulated martian surface conditions (see

Section 5.1), meaning that if alunite is present in this outcrop, we should also expect to see contributions from absorptions at 1.78, 2.16, 2.18, 2.32 and 2.51 μm. However, in these spectra there is only weak evidence for features at those positions.

A deep feature at 1.86 μm is a major absorption of the ferric sulphate jarosite (including K- and Na- jarosite). It appears in a moderately shallow instance in several region A spectra representing exposures of the eastern low-level ILDs (spectra 8158_3 and 8158_4) and in two spectra from region B (A85F_1 and A85F_6).

Absorptions centred approximately at 1.96 μm, 2.02 μm and 2.06 μm could be the 2 μm feature which is common to virtually all spectra in this study. However, it should be noted that this region is subject to an artefact introduced by the 'volcano-scan'

atmospheric correction procedure, which forms a dip of ~5% amplitude from 1.9 to 2.1 μm (Morgan, 2009).

On the ascending limb of this artefact, the depth of the ~2.09 μm absorption is used by spectral summary parameter BD2100 to indicated monohydrated minerals, such as kieserite (Bishop et al., 2009).

Shallow absorptions at 2.21 μm and 2.26 μm, characteristic of gypsum and jarosite, always appear together and, in region A are most prominent in the lower elevation ILDs (spectra 7E16_4, 7E16_5, 7E16_6, 8158_2 and 8158_3). In region B they are most prominent in three spectra of the ILD (A85F_1, 2 and 3) and one that represents the slopes of the chaotic mound (A85F_6). Increased band depth at 2.21 μm is characteristic of Al–OH minerals (Pelkey et al., 2007), however gypsum also has a doublet comprising shallow absorptions at 2.21 μm and 2.26 μm.

The 2.13 μm absorption seen in spectra of many chaotic mounds and ILDs is likely due to the presence of kieserite, since kieserite's absorptions at 1.96 μm and 2.06 μm are also seen in these spectra as well as a 2.09 μm absorption which could be indicative of the presence of szomolnokite (Bishop et al., 2009).

The spectral summary parameter SINDEX represents the band depth of the 2.4 μm absorption and indicates the presence of sulphate minerals. This signature is strong in region A in high albedo ILDs on slopes (spectra 7E16_1, 7E16_2 and 8158_2) and in region D in spectra covering the bench of the main deposit (B4C8_1), a stratigraphically lower light-toned bed (C034_1) and several outcrops in scattered knobs (C034_4 and C034_5).

A shallow, narrow absorption at 2.53 μm could suggest the presence of a variety of polyhydrated sulphates (botryogen, starkeyite, ferricopiapite) or kieserite. It is present in regions A and B in the spectra of the high albedo light-toned material on ILDs and in bright outcropping material in the chaotic mound slopes, while it is present in virtually all spectra in region D.

5. Discussion of interpretation of CRISM spectral data

Through analysis of CRISM data in Iani Chaos we find diagnostic absorptions for gypsum and kieserite, several sets of features that could be indicative of alunite and jarosite and a range of weak absorptions possibly associated with the presence of polyhydrated sulphates (see Fig. 17).

Our method relies on manual comparison of absorption position, shape and depth with those in spectral libraries. For CRISM data in Iani Chaos, we found this method to yield the most conclusive results. Linear unmixing of spectra, to quantify relative spectral contributions from different phases, produced inconclusive results. This may have been due to limitations in this situation: Spectral signatures of phases that contain OH and H_2O may be subject to alteration due to exposure to martian surface conditions (Cloutis et al., 2008) (also see Section 5.1). This can cause laboratory reference spectra that typically acquired for phases exposed only to ambient conditions (~20 °C, 1 bar), to ill-represent actual reflectance properties of minerals on the martian surface. In addition, many hydrated sulphate phases that are likely to be observed possess absorption bands that overlap, which could cause false positives in un-mixing methods.

5.1. Detection of gypsum

Gypsum spectral signatures were detected by Gendrin et al. (2005) on ILDs in western region A and on benches on the eastern portions of the main ILD in region D. We confirm these detections and note that gypsum is only able to be produced at temperatures <60 °C. Above this threshold anhydrite is formed (Catling et al.,
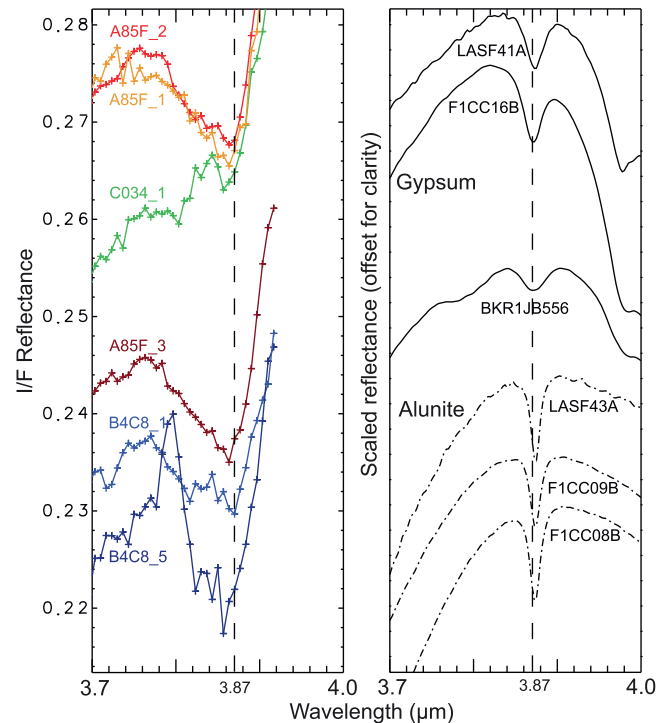
Fig. 18. Comparison of spectra from ILDs in regions B and D in the 3.7–4.0 μm to RELAB spectra of gypsum and alunite. A characteristic absorption at 3.87 μm is shown by both minerals but is not shared by any other sulphates in the available RELAB spectra.

2006), which perhaps places an upper temperature limit on the genetic conditions of gypsum-bearing ILDs.

Gypsum that forms veins and cement in local bedrock was discovered by the Opportunity Rover in Endeavour Crater at Meridiani Planum, approximately 500 km East of Iani Chaos. It is likely to have been precipitated from relatively dilute, moderate temperature fluids, perhaps generated in local sulphate-rich Noachian crust (Squyres et al., 2012). If gypsum that we detect in Iani Chaos is in a similar form, its presence would indicate formation by non-cryogenic, moderate pH fluids, which may have been associated with transiently habitable conditions. In that case, the timing and conditions of modelled groundwater upwelling events at Meridiani Planum (Andrews-Hanna et al., 2010), could be related to those that influenced gypsum-bearing ILDs in Iani Chaos. However, the formation mode of gypsum in Iani Chaos ILDs is unlikely to be conclusively determined without in situ stratigraphic and sedimentary analysis.

Gypsum is characterised by a triplet of absorptions of decreasing intensity centred around 1.44, 1.49 and 1.53 μm (due to O–H stretches), a band near 1.75 μm (due to an OH combination), a doublet with absorption centres near 1.94 and 1.97 μm (caused by H_2O combinations), a complex feature with two minima centred at 2.22 μm and 2.27 μm (due to H_2O combinations/S–O stretching overtones) and a shallow absorption near 2.48 μm caused by an S–O stretching combination (Cloutis et al., 2008, 2006; Gendrin et al., 2005). The absence of any discernible absorption at 1.75 μm may be accounted for by the effects of long-term exposure of gypsum to martian surface conditions. The reduction in depth of absorption bands as well as the shifting of some features to shorter wavelengths was found to affect Fe^{3+} and H_2O bearing sulphates when they were exposed to simulated martian surface pressure, temperature and ultraviolet conditions. In experiment SPT127 (Run 1) of Cloutis et al. (2008) the 1.75 μm band was seen to disappear entirely. Bands between 2.0 and 2.5 μm were found to be

particularly susceptible to spectral shifting, making more plausible our assignment of absorptions at 2.21 μm and 2.26 μm to those of gypsum at 2.22 μm and 2.27 μm, respectively (Figs. 14 and 17). With these effects known, it is apparent that a large proportion of spectra in Fig. 16 may show evidence for the presence of gypsum in ILDs in regions B and D.

Three spectra from the main ILD in CRISM cube A85F and three spectra from cubes C034 and B4C8 representing the main ILD and a dispersed layered outcrop away from the main ILD show a moderate absorption at 3.87 μm (Fig. 18). This is not shared by the other spectra in these cubes and is commensurate with absorptions seen at this position in gypsum (RELAB spectra F1CC16B and LASF41A) and alunite (RELAB spectra F1CC08B, F1CC09B and LASF43A). No other sulphate minerals in RELAB spectral libraries were found to possess this absorption.

5.2. Detection of kieserite

Spectral evidence for kieserite that we report for ILDs in regions A, B and D comprises the mutual presence of absorptions at 2.09, 2.13 and 2.53 μm. Kieserite ($MgSO_4 \cdot H_2O$), when exposed to water is converted to hexahydrite ($MgSO_4 \cdot 6H_2O$) and epsomite ($MgSO_4 \cdot 7H_2O$). However, upon further desiccation, these minerals are not converted back to kieserite, unless they are subject to heating and burial (Roach et al., 2009). Gendrin et al. (2005) suggest that kieserite is not likely to be present in deposits that have experienced exposure to water after their initial formation. We conclude that deposits in which kieserite is present have probably not been subject to multiple aqueous episodes unless the kieserite is the result of burial and heating of deposits that originally contained polyhydrated sulphates.

5.3. Absorptions at 1.07, 1.31 and 1.57 μm

A suite of absorptions that tend to occur together, but not individually, in ILDs of Iani Chaos include those at 1.07 μm, 1.31 μm and 1.57 μm. Massé et al. (2010) also detect absorptions at these positions in their analysis of sulphate deposits thought to be sublimation tills surrounding the north polar cap. Both water ice and CO_2 ice show absorptions at 1.07 and 1.31 μm (Pelkey et al., 2007; Massé et al., 2010). However the stability of surface water–ice at equatorial latitudes is unlikely and Massé et al. (2010) conclude that they are not instrumental or atmospheric artefacts could be attributed to other components.

There are large variations in the strength of the features between spectra from the same observation. Some regions of interest do not exhibit the absorptions, while others in the same observation show it clearly. Band depth is independent of column position in unprojected cubes, i.e. spectra from regions of interest in the same column show different feature strengths. This reinforces the view that they are probably due to surface mineralogy, since instrumental artefacts or atmospheric artefacts would likely have a homogenous effect on the entire field of view. Misinterpretation of these features remains a risk because (1) although feature strengths vary across observation footprints, even sometimes with fixed column number, we cannot fully discount the possibility that they are caused by atmospheric aerosols, since the equatorial CRISM observations that we use could be susceptible to influence by aphelion water–ice clouds, and (2) there remains a paucity in understanding and quantification of spectral degradation of hydrated salts under martian surface conditions over geologic time (Cloutis et al., 2008).

However, we find that these absorptions are also exhibited by ammonium sulphates such as mascagnite ($(NH_4)_2SO_4$) and letovicite ($(NH_4)_3H(SO_4)_2$). The presence of nitrogen-bearing minerals on Mars is ill-constrained (Mancinelli and Banin, 2003), but Quinn et al. (2011) report detection of ammonium in concentrations of 0.86×10^{-7} moles NH_4^+ cm^{-3} in soils at the Phoenix landing site. Isotopic analysis of nitrogen in SNCs suggests that Mars could have once harboured 250–600 mbars of nitrogen and that steady-state fractionation from $^{14/15}N_{SNC} = 278$ to $^{14/15}N_{atm} = 170 \pm 15$ (Fox, 1993; Wallis, 1989) was facilitated by decomposition of near-surface nitrates during impact shock heating and subsequent equilibrium reactions between the dissociated atoms (Mancinelli and McKay, 1988; Navarro-Gonzalez et al., 2001) leading to atmospheric loss.

Manning et al. (2007) estimate that roughly a quarter of nitrates evaded impact dissociation and remained fixed in the upper crust, becoming susceptible to dissolution by groundwater and involvement with the hydrological cycle. In a hypothesised scenario envisaged by Manning et al. (2007), a ~1.6% mass fraction of N in the top 100 m of martian crust, concentrated by groundwater redistribution, could be influenced by near-surface magmatism. In a sulphur-rich setting, ammonium sulphates such as mascagnite ($(NH_4)_2SO_4$) or letovicite ($(NH_4)3H(SO_4)_2$) could form. Both these phases show absorptions at 1.07 μm, 1.31 μm and 1.57 μm (RELAB library spectra LASF15B, LASF17A and LASF17B as plotted in Fig. 17) that we observe in CRISM spectra (Figs. 14 and 16). These phases typically form naturally on Earth at volcanic fumaroles such as those formed by the Campi Flegrei volcanic system, Italy (Valentino et al., 1999) or together with perchlorates in the Atacama desert (Ericksen, 1981). However, the rapidity with which ammonium phases should oxidise in the prevailing oxidising environment of Mars bears consideration.

6. Discussion on the origins of ILDs

6.1. Groundwater in Iani Chaos?

The correlation of distinct stratigraphic levels in region A with distinct bulk hydration states (Fig. 15), mineralogies (Figs. 13 and 14) and surface textures (Fig. 6) could imply (1) saturation of the stratigraphic column in central Iani Chaos to different elevations after ILD formation or (2) formation of ILDs by different processes/conditions.

Any aqueous recharge event could cause secondary diagenesis and may change the bulk properties of a rock unit, both mineralogically and thermophysically. Dissolution of existing minerals and crystallisation of new phases in pore space, such as that thought to have occurred at Meridiani Planum (Catling, 2004; Grotzinger et al., 2005; McLennan et al., 2005; Squyres et al., 2004b; Sefton-Nash and Catling, 2008; Andrews-Hanna et al., 2007) would cause cementation of the unit, leading to changes in density, porosity and thermal conductivity. While we find a heterogeneous distribution of spectral signatures in Iani Chaos (Figs. 13 and 14), our thermal inertia data for region A (Figs. 4 and 5) indicates similar thermophysical properties for ILDs in this region, although this does not rule out the possibility that different deposits have been modified to varying extents by diagenesis.

Our spectral analysis shows different hydration states for different strata in central Iani Chaos (Fig. 15). This could suggest either that individual ILD beds formed in chemically different environments or that only the stratigraphically lower beds have been modified by aqueous recharge since their formation. The latter scenario would require groundwater activity after initial ILD formation, but the timing can only be constrained to after outflow channel formation in the late Amazonian (~2.5–2.9 Ga) (Warner et al., 2011), since it is possible that aqueous recharge of ILDs was caused by late stage outflow channel groundwater effusion.

Analysis of MOLA data suggests that curvilinear depressions proximal to Iani Chaos could represent sub-surface conduits for

hydraulic transmission between regions of chaotic terrain (Harrison, 2009). Preliminary mapping of these depressions to the immediate west shows that a network of N–S oriented conduits linking Aureum and Hydaspis Chaos may be connected to several E–W conduits that terminate in western Iani Chaos. These observations are consistent with aquifer recharge from distal sources that may have been required to supply the necessary water to form Iani Chaos (Warner et al., 2011), but it remains unclear whether groundwater involved in forming the later stages of Iani Chaos could have influenced the hydration states of ILDs during their formation.

An alternate hypothesis is the formation of ILDs by acid weathering in massive dust-ice deposits (Niles and Michalski, 2009), which would not necessarily require groundwater mobility. In that case, differences between different ILDs in Iani Chaos would be facilitated by their formation in a chemically isolated system where the ILDs final composition is dictated by the initial composition of successive buried layers of dust, ice and volcanic aerosols laid down over obliquity cycles. Correlation of decameter-scale layering in ILDs with the periodicity of obliquity cycles has been noted for other deposits in Becquerel crater (Bridges et al., 2008; Lewis et al., 2008).

6.2. Aeolian weathering

Deposits in regions B and D show surface erosional features that indicate extensive sculpting by the wind over geologic timescales (i.e. yardangs, aeolian fretting and scalloped surface textures). ILDs in region B, particularly the higher elevation deposit, B1, shows a strong NW–SE orientation of ridges that we interpret to be yardangs (Fig. 8). Their trend is commensurate with the direction of the near-surface equatorial ('trade-wind') branch of the Hadley circulation (Fenton and Richardson, 2001). The direction of this circulation reverses at opposing seasons, but at Iani Chaos, remains in a NW–SE trend. According to the orientation of bright streaks observed in Viking imagery this appears to be the current prevailing wind regime (Magalhaes, 1987).

Conversely, the main ILD in region D shows aeolian fretting and yardangs that require a NE–SW trending wind orientation (Figs. 11 and 12). While apparently not commensurate with prevailing wind conditions, we note that these features could be caused by 'return flow' of the cross-equatorial boundary current on the eastern flanks of Tharsis during the solstices (Joshi et al., 1995).

6.3. Salt diapirism?

If, during burial, ILDs possessed a sulphate-rich mineralogy then they would have a lower density than surrounding materials, perhaps instigating buoyancy-driven tectonics. Salt diapirism has been hypothesised to be a viable formation method for the dome-like morphology of many ILDs (Baioni and Wezel, 2010). Milliken et al. (2007) note that geomorphic similarities are apparent between features formed by salt-tectonism on Earth (Great Kavir, Iran) and similar features in Melas and Candor Chasma in central Valles Marineris on Mars. Specifically, rootless folds, disharmonic folding and dome-like morphology are reported to be common to these locations.

ILDs in region B show asymmetric dome morphologies with dimensions comparable to those modelled by Beyer et al. (2000) and within the size-range of terrestrial salt-diapirs. However, a dome-shaped surface expression does not require internal deformation driven by buoyancy effects, and may be due only to the draping of ILDs over pre-existing chaotic mounds. Dipping layers exposed in region D appear largely planar and show no evidence for a dome-like structure of the ILD.

6.4. Spring deposits?

Spring deposits should display strong lateral and vertical facies variations (Baioni and Wezel, 2010) and Fig. 6b shows this kind of behaviour in the flat-lying layered units in central region A. In the relatively flat topographic depression the lobate nature of some bed terminations bear some resemblance to modern travertine fans (Rossi et al., 2008, Fig. 2c). Furthermore, the layered deposits here appear to embay topographic maxima in the stratigraphically subordinate terrain (Gilmore and Greenwood, 2009). However, ILDs elsewhere in Iani Chaos do not exhibit these traits.

7. Conclusions

Analysis of CRISM spectra of ILDs in Iani Chaos reveals a suite of spectral features indicating the presence of a suite of mono- and polyhydrated sulphate minerals. We observe the spectral characteristics of gypsum and kieserite in the ILDs of regions A, B and D. Incomplete sets of spectral features that could indicate alunite and jarosite are also present in these regions. We identify absorptions at 1.07 μm, 1.31 μm and 1.57 μm in the spectra of many ILDs. The first two could be attributed to water–ice and CO_2 ice (Pelkey et al., 2007; Massé et al., 2010), although the presence of either ice on the surface at equatorial latitudes is unlikely, implying cause by aerosols, which we cannot definitively rule out. Previous work has not determined the cause of a 1.57 μm absorption (Massé et al., 2010). There is similarity between these three features and those shown by the ammonium sulphates, mascagnite and letovicite. We find the presence of ammonium sulphate in the martian crust not implausible.

Sub-decametre layering in ILDs is indicative of their deposition by cyclical processes. These could be aeolian in origin (Bridges et al., 2008; Lewis et al., 2008), but could also be caused by successive deposition of sediment-bearing ice-deposits over orbital obliquity cycles (Catling et al., 2006; Niles and Michalski, 2009). In any case, this study suggests that ILDs were deposited in topographic depressions after the formation of Iani Chaos.

ILDs in Iani Chaos span a wide range of elevations and do not consistently occupy the lowest in Iani Chaos. The upper limit of their elevation also lies above the entry point to Ares Vallis, as observed by Warner et al. (2011) (see Fig. 3). We find no evidence in the morphology of ILDs for erosion by significant overland flow and therefore conclude that any diagenesis may have been facilitated either by localised melting in ice deposits (Niles and Michalski, 2009) or elevation of the local water table via topographic pumping (Grindrod and Balme, 2010). Regional elevation of the water table (Andrews-Hanna et al., 2007) in Iani Chaos may have occurred prior to ILD formation, but has probably not influenced ILD mineralogy because existing topography does not allow for ponding to sufficient elevations to alter ILDs. We agree with Warner et al. (2009) and Warner et al. (2011), who rule out a lacustrine origin for ILDs.

Analysis of hydration state over stratigraphic level suggests that ILDs in central Iani Chaos (Region A) may have been subject to multiple episodes of saturation. Interaction of ILDs with fluids could have caused dissolution of existing minerals or crystallisation of new phases in pore space. As a result, the range of physical appearances and thermophysical properties shown by ILDs may represent differing mineral assemblages, porosities and degrees of cementation. In addition, boundaries between phase-assemblages in ILD sequences could represent areas affected by aqueous episodes of different durations, paleo-water table heights or simply be the result of chemical isolation during formation in massive ice deposits (Niles and Michalski, 2009).

Only ILD B1 shows a dome-shaped morphology that could support influence on its shape by salt tectonism. But the planar layering of ILDs in regions A and D favour emplacement that is not influenced by salt tectonics. We note that ILDs in region B are situated at the lowest elevation of all ILDs in Iani Chaos (Fig. 3). If buried, these deposits would have been the most susceptible to buoyancy effects compared to other ILDs in Iani Chaos.

The lack of small craters and extensive aeolian erosion features exhibited by ILDs in Iani Chaos suggests that they have been relatively recently exposed and are being actively eroded by the wind. Extensive aeolian modification throughout the Amazonian has probably dominated the most recent geologic history of ILDs (~20–100 Ma according to crater retention ages calculated by Warner et al. (2011)), obscuring their contacts with the surrounding terrain and adding morphological complication to their surface textures.

Acknowledgments

References

Andrews-Hanna, J.C., Phillips, R.J., Zuber, M.T., 2007. Meridiani Planum and the global hydrology of Mars. Nature 446 (7132), 163–166.

Andrews-Hanna, J.C., Zuber, M.T., Arvidson, R.E., Wiseman, S.M., 2010. Early Mars hydrology: Meridiani playa deposits and the sedimentary record of Arabia Terra. J. Geophys. Res. 115 (E06002), 1–22.

Baioni, D., Wezel, F.C., 2010. Morphology and origin of an evaporitic dome in the eastern Tithonium Chasma, Mars. Planet. Space Sci. 58, 847–857.

Baker, V., Milton, D.J., 1974. Erosion by catastrophic floods on Mars and Earth. Icarus 23, 27–41.

Bandfield, J.L., 2003. martian global surface mineralogy from the thermal emission spectrometer: Surface emissivity, mineral map and spectral endmember data products. In: Sixth International Conference on Mars. Abstract 3052.

Beyer, R.A., Melosh, H.J., McEwen, A.S., Lorenz, R.D., 2000. Salt diapirs in Candor Chasma, Mars? Lunar Planet. Sci. XXXI. Abstract 2022.

Bibring, J.-P. et al., 2007. Coupled ferric oxides and sulfates on the martian surface. Science 317, 1206–1210.

Bibring, J.-P., Squyres, S.W., Arvidson, R.E., 2006. Merging views on Mars. Science 313 (5795), 1899–1901.

Bishop, J.L. et al., 2009. Mineralogy of Juventae Chasma: Sulfates in the light-toned mounds, mafic minerals in the bedrock, and hydrated and hydroxylated ferric sulfate on the plateau. J. Geophys. Res. – Planets 114 (E00D09), 1–23.

Bridges, J.C., Kim, J.-R., Tragheim, D.G., Muller, J.-P., Balme, M.R., Pullan, D., 2008. Sedimentary rocks in Becquerel crater: Origin as polar layered deposits during high obliquity. Lunar Planet. Sci. XXXIX. Abstract 1913.

Burch, D.E., Gryvnak, D.A., Patty, R.R., 1968. Absorption of infrared radiation by CO_2 and H_2O. II. Absorption by CO_2 between 8000 and 10,000 cm^{-1} (1–1.25 Microns). J. Opt. Soc. Am. 58 (3), 335–341.

Carr, M.H., 2001. Mars Global Surveyor observations of martian fretted terrain. J. Geophys. Res. 106 (E10), 23,571–23,593.

Carr, M.H., Head, J.W., 2010. Geologic history of Mars. Earth Planet. Sci. Lett. 294 (3-4), 185–203.

Catling, D.C., 2004. Planetary science: On Earth, as it is on Mars? Nature 429 (6993), 707–708.

Catling, D.C., Moore, J.A., 2003. The nature of coarse-grained crystalline hematite and its implications for the early environment of Mars. Icarus 165 (2), 277–300.

Catling, D.C., Wood, S.E., Leovy, C., Montgomery, D.R., Greenberg, H.M., Glein, C.R., Moore, J.M., 2006. Light-toned layered deposits in Juventae Chasma, Mars. Icarus 181 (1), 26–51.

Chapman, M.G., Tanaka, K.L., 2001. Interior trough deposits on Mars: Sub-ice volcanoes? J. Geophys. Res. 106 (E5), 10087–10100.

Clark, B.C., Van Hart, D.C., 1981. The salts of Mars. Icarus 45, 370–378.

Clark, R.N., King, T.V.V., Klejwa, M., Swayze, G.A., 1990. High spectral resolution reflectance spectroscopy of minerals. J. Geophys. Res. 95 (B8), 12653–12680.

Cloutis, E.A., Hawthorne, F.C., Mertzman, S.A., Krenn, K., Craig, M.A., Marcino, D., Methot, M., Strong, J., Mustard, J.F., Blaney, D.L., Bell, J.F., Vilas, F., 2006. Detection and discrimination of sulfate minerals using reflectance spectroscopy. Icarus 184, 121–157.

Cloutis, E.A., Craig, M.A., Kruzelecky, R.V., Jamroz, W.R., Scott, A., Hawthorne, F.C., Mertzman, S.A., 2008. Spectral reflectance properties of minerals exposed to simulated Mars surface conditions. Icarus 195 (1), 140–168.

Dalton, J.B.I., Pitman, K.M., Jamieson, C.S., Noe Dobrea, E.Z., 2011. Spectral properties of hydrated sulfate minerals on Mars. EPSC-DPS Joint Meeting.

Ericksen, G.E., 1981. Geology and Origin of the Chilean Nitrate Deposits. Professional Paper, United States Geological Survey.

Farrand, W.H., Glotch, T.D., Rice Jr., J.W., Hurowitz, J.A., Swayze, G.A., 2009. Discovery of jarosite within the Mawrth Vallis region of Mars: Implications for the geologic history of the region. Icarus 204, 478–488.

Fenton, L.K., Richardson, M.I., 2001. Martian surface winds: Insensitivity to orbital changes and implications for aeolian processes. J. Geophys. Res. 106 (E12), 32,885–32,902.

Fox, J.L., 1993. The production and escape of nitrogen atoms on Mars. J. Geophys. Res. 98, 3297–3310.

Fueten, F. et al., 2008. Stratigraphy and structure of interior layered deposits in west Candor Chasma, Mars, from High Resolution Stereo Camera (HRSC) stereo imagery and derived elevations. J. Geophys. Res. 113 (E100008), 1–19.

Fueten, F., Stesky, R.M., MacKinnon, P., 2005. Structural attitudes of large scale layering in Valles Marineris, Mars, calculated from Mars Orbiter Laser Altimeter data and Mars Orbiter Camera imagery. Icarus 175, 68–77.

Gendrin, A. et al., 2005. Sulfates in martian layered terrains: The OMEGA/Mars express view. Science 307, 1587–1591.

Gilmore, M. S., Greenwood, J. P., 2009, Gypsum and associated sulfates in Iani Chaos, Mars., Eos Trans. AGU, 90 (52), Fall Meet. Suppl., Abstract P21C-04.

Glotch, T.D., Rogers, A.D., 2007. Evidence for aqueous deposition of hematite- and sulfate-rich light-toned deposits in Aureum and Iani Chaos, Mars. J. Geophys. Res. 112 (E06001), 1–11.

Grindrod, P.M., Balme, M.R., 2010. Groundwater processes in Hebes Chasma, Mars. Geophys. Res. Lett. 37 (L13202), 1–5.

Grindrod, P.M., West, M., Warner, N.H., Gupta, S., 2012. Formation of an Hesperian-aged sedimentary basin containing phyllosilicates in Coprates Catena, Mars. Icarus 218, 178–195.

Grotzinger, J.P. et al., 2005. Stratigraphy and sedimentology of a dry to wet eolian depositional system, Burns formation, Meridiani Planum, Mars. Earth Planet. Sci. Lett. 240 (1), 11–72.

Gwinner, K. et al., 2010. Topography of Mars from global mapping by HRSC high-resolution digital terrain models and orthoimages: Characteristics and performance. Earth Planet. Sci. Lett. 294, 506–519.

Harrison, K.P., 2009. An alternative view of martian chaotic terrain formation. In: Lunar Planet. Sci. XXXX. Abstract 1743.

Harrison, K.P., Grimm, R.E., 2008. Multiple flooding events in martian outflow channels. J. Geophys. Res. 113 (E02002), 1–11.

Joshi, M.M., Lewis, S.R., Read, P.L., Catling, D.C., 1995. Western boundary currents in martian atmosphere: Numerical simulations and observational evidence. J. Geophys. Res. – Planets 100 (E3), 5485–5500.

Kieffer, H.H., Martin, T.Z., Peterfreund, A.R., Jakosky, B.M., 1977. Thermal and albedo mapping of Mars during the viking primary mission. J. Geophys. Res. 82 (28), 4249–4291.

Kirk, R.L. et al., 2008. Ultrahigh resolution topographic mapping of Mars with MRO HiRISE stereo images: Meter-scale slopes of candidate Phoenix landing sites. J. Geophys. Res. 113 (E00A24), 1–31.

Komatsu, G., Ori, G.G., Ciarcelluti, P., Litasov, Y.D., 2004. Interior layered deposits of Valles Marineris, Mars: Analogous subice volcanism related to Baikal Rifting, Southern Siberia. Planet. Space Sci. 52 (1–3), 167–187.

Leverington, D.W., 2011. A volcanic origin for the outflow channels of Mars: Key evidence and major implications. Geomorphology 132, 51–75.

Lewis, K.W., Aharonson, O., Grotzinger, J.P., Kirk, R.L., McEwen, A.S., Suer, T.-A., 2008. Quasi-periodic bedding in the sedimentary rock record of Mars. Science 322, 1532–1535.

Loizeau, D., Mangold, N., Poulet, F., Ansan, V., Hauber, E., Bibring, J.-P., Gondet, B., Langevin, Y., Masson, P., Neukum, G., 2010. Stratigraphy in the Mawrth Vallis region through OMEGA, HRSC color imagery and DTM. Icarus 205 (2), 396–418.

Lucchitta, B.K., 1990. Young volcanic deposits in the Valles Marineris, Mars? Icarus 86, 476–509.

Magalhaes, J.A., 1987. The martian Hadley circulation: Comparison of 'viscous' model predictions to observations. Icarus 70, 442–468.

Malin, M.C., Edgett, K.S., 2000. Sedimentary rocks of early Mars. Science 290, 1927–1937.

Mancinelli, R.L., Banin, A., 2003. Where is the nitrogen on Mars? Int. J. Astrobiol. 2 (3), 217–225.

Mancinelli, R.L., McKay, C.P., 1988. The evolution of nitrogen cycling. Origins Life 18, 311–325.

Manning, C.V., McKay, C.P., Zahnle, K.J., 2007, Nitrates on Mars: Evidence from the 15/14N isotopic ratio., Eos Trans. AGU, Fall Meet. Suppl., Abstract P13D-1556.

Marchenko, A.G., Basilevsky, A.T., Hoffmann, H., Hauber, E., Cook, A.C., Neukum, G., 1998. Geology of the common mouth of the Ares and Tiu Valles, Mars. Sol. Syst. Res. 32 (6), 425–452.

Massé, M., Bourgeois, O., Le Mouélic, S., Verpoorter, C., Le Deit, L., Bibring, J.P., 2010. Martian polar and circum-polar sulfate-bearing deposits: Sublimation tills derived from the North Polar Cap. Icarus 209, 434–451.

McLennan, S.M. et al., 2005. Provenance and diagenesis of the evaporite-bearing Burns formation, Meridiani Planum, Mars. Earth Planet. Sci. Lett. 240 (1), 95–121.

Milliken, R.E., Grotzinger, J., Beyer, A., Murchie, S., McEwen, A.S., Team, T.C.S., 2007. Evidence for salt tectonics in Valles Marineris, Mars. Seventh Int. Conf. Mars. LPI Cont. No. 1353, p.3383.

Montgomery, D.R., Gillespie, A., 2005. Formation of martian outflow channels by catastrophic dewatering of evaporite deposits. Geology 33 (8), 625–628.

Morgan, F., 2009. CRISM 2 micron artifact. Tech. Rep., Lunar and Planetary Institute.

Murchie, S. et al., 2009. Evidence for the origin of layered deposits in Candor Chasma, Mars, from mineral composition and hydrologic modelling. J. Geophys. Res. 114 (E00D05), 1–15.

Navarro-Gonzalez, R., McKay, C.P., Mvondo, D.N., 2001. A possible nitrogen crisis for Archean life due to reduced nitrogen fixation by lightning. Nature 412, 61–64.

Nedell, S.S., Squyres, S.W., Andersen, D.W., 1987. Origin and evolution of the layered deposits in the Valles Marineris, Mars. Icarus 70 (3), 409–414.

Niles, P.B., Michalski, J., 2009. Meridiani Planum sediments on Mars formed through weathering in massive ice deposits. Nat. Geosci. 2, 215–220.

Noe Dobrea, E.Z., Poulet, F., Malin, M.C., 2006. Omega analysis of light-toned layered outcrops in the chaotic terrain of the eastern Valles Marineris region. Lunar Planet. Sci. XXXVII. Abs. 2068.

Okubo, C.H., 2010. Structural geology of Amazonian-aged layered sedimentary deposits in southwest Candor Chasma, Mars. Icarus 207, 210–225.

Ori, G.G., Mosangini, C., 1998. Complex depositional systems in Hydraotes Chaos, Mars: An example of sedimentary process interactions in the martian hydrological cycle. J. Geophys. Res. 103 (E10), 22713–22723.

Pacifici, A., Komatsu, G., Pondrelli, M., 2008. Geological evolution of Ares Vallis on Mars: Formation by multiple events of catastrophic flooding, glacial and periglacial processes. Icarus 202, 60–77.

Pelkey, S.M. et al., 2007. CRISM multispectral summary products: Parameterizing mineral diversity on Mars from reflectance. J. Geophys. Res. 112 (E08), 1–18.

Peterson, C., 1981. A secondary origin for the central plateau of Hebes Chasma. Lunar and Plan. Sci. XII. Proceedings. Sec. 2. (A82-31677 15-91) New York and Oxford, Pergamon Press. 1459–1471.

Piqueux, S., Christensen, P.R., 2008. North and south subice gas flow and venting of the seasonal caps of Mars: A major geomorphological agent. J. Geophys. Res. 113 (E06005), 1–16.

Presley, M.A., Christensen, P.R., 1997. Thermal conductivity measurements of particulate materials 2. Results. J. Geophys. Res. 102 (E3), 6551–6566.

Putzig, N.E., Mellon, M.T., Kretke, K.A., Arvidson, R.E., 2005. Global thermal inertia and surface properties of Mars from the MGS mapping mission. Icarus 173, 325–341.

Quinn, R.C., Chittenden, J.D., Kounaves, S.P., Hecht, M.H., 2011. The oxidation–reduction potential of aqueous soil solutions at the Mars Phoenix landing site. Geophys. Res. Lett. 38 (L14202), 1–4.

Roach, L.H. et al., 2009. Testing evidence of recent hydration state change in sulfates on Mars. J. Geophys. Res. 114 (E00D02), 1–13.

Rossi, A.P. et al., 2008. Large-scale spring deposits on Mars? J. Geophys. Res. 113 (E08016), 1–17.

Sefton-Nash, E., Catling, D.C., 2008. Hematitic concretions at Meridiani Planum, Mars: Their growth timescale and possible relationship with iron sulfates. Earth Planet. Sci. Lett. 269, 365–375.

Sharp, R.P., 1973. Mars: Fretted and chaotic terrains. J. Geophys. Res. 20, 4073–4083.

Smith, M.D., Bandfield, J.L., Christensen, P., Richardson, M.I., 2003. Thermal Emission Imaging System (THEMIS) infrared observations of atmospheric dust and water ice cloud optical depth. J. Geophys. Res. 108 (E11), 5115.

Sowe, M., 2009. Interior Layered Deposits in Chaotic Terrains on Mars. Ph.D. Thesis, Freie Universitat Berlin.

Squyres, S.W. et al., 2004a. The opportunity Rover's Athena science investigation at Meridiani Planum, Mars. Science 306 (5702), 1698–1703.

Squyres, S.W. et al., 2004b. In situ evidence for an ancient aqueous environment at Meridiani Planum, Mars. Science 306 (5702), 1709–1714.

Squyres, S.W. et al., 2012. Ancient impact and aqueous processes at Endeavour Crater, Mars. Science 336, 570–576.

Thomas, M., Clarke, J.D.A., Pain, C.F., 2005. Weathering, erosion and landscape processes on Mars identified from recent rover imagery, and possible Earth analogues. Aust. J. Earth Sci. 52, 365–378.

Valentino, G.M., Cortecci, G., Franco, E., Stanzione, D., 1999. Chemical and isotopic compositions of minerals and waters from the Campi Flegrei volcanic system, Naples, Italy. J. Volcan. Geotherm. Res. 91, 329–344.

Wallis, M.K., 1989. C, N, O isotope fractionation on Mars: Implications for crustal H2O and SNC meteorites. Earth Planet. Sci. Lett. 93, 321–324.

Warner, N.H. et al., 2011. Constraints on the origin and evolution of Iani Chaos, Mars. J. Geophys. Res. – Planets 116 (E06003), 1–29.

Warner, N., Gupta, S., Muller, J.-P., Kim, J.-R., Lin, S.-Y., 2009. A refined chronology of catastrophic outflow events in Ares Vallis, Mars. Earth Planet. Sci. Lett. 288 (1-2), 58–69.

Weitz, C.M., Bishop, J.L., Thollot, P., Mangold, N., Roach, L.H., 2011. Diverse mineralogies in two troughs of Noctis Labyrinthus, Mars. Geology 39 (10), 899–902.

Wood, S.E., 2011. A general analytic model for the thermal conductivity of loose indurated or icy planetary regolith. Lunar Planet. Sci. XXXXII, Abs. 2795.

Zuber, M.T. et al., 1992. The Mars observer laser altimeter investigation. J. Geophys. Res. 97 (E5), 7781–7797.